

Received 21 May 2025, accepted 12 June 2025, date of publication 17 June 2025, date of current version 15 July 2025.

Digital Object Identifier 10.1109/ACCESS.2025.3580420



Fractional Order Approach for Conical Active Magnetic Bearings Under Time Delay and Supply Faults

DUC THINH LE^{®1}, DANH GIANG NGUYEN^{®2,3}, THE TAI TA², TUNG LAM NGUYEN^{®2}, (Senior Member, IEEE), MINH VU NHAT^{®4,5}, AND DANH HUY NGUYEN^{®2}

¹Faculty of Electrical and Electronics Engineering, Thuyloi University, Dong Da, Hanoi 100000, Vietnam

Corresponding author: Danh Huy Nguyen (huy.nguyendanh@hust.edu.vn)

This work was supported by Hanoi University of Science and Technology (HUST) under Project T2023-PC-029.

ABSTRACT A conical magnetic bearing system (CAMBs) has emerged as a promising solution for various applications relying on magnetic force, thanks to its unique geometry, which reduces the need for multiple active magnets and reduces energy consumption for supporting maximum loads and lower copper losses. Due to the inherent nonlinearity and coupling characteristics of the 5-DOF CAMBs, a detailed mathematical model as well as the design of a highly accurate control scheme are essential, especially under the influence of external disturbances, unbalance disturbances, and supply faults. The proposed mathematical model integrates both the electrical and mechanical systems, making it subject to mismatched and matched disturbances. Furthermore, the system also accounts for issues such as supply faults, supply saturation, and time delays in both power supplies and sensors. To address these challenges, a cascade control structure for CAMBs is proposed, comprising an outer loop and an inner loop. The outer loop employs fractional order sliding mode control (FOSMC) to regulate the rotor's displacement and rotational angle. Meanwhile, the inner loop utilizes a fractional-order PID (FOPID) controller to control coil currents, effectively mitigating the influence of eddy currents and the time delay issues associated with power supplies and sensors. Furthermore, disturbances are addressed through a hybrid extended state observer (ESO) structure, where a fast ESO is implemented in the inner loop, while a slow ESO is applied to the outer loop to observe mismatched and matched disturbances. Overall stability of the closed-loop system control is mathematically proven. Finally, the simulation evaluation using particle swarm optimization for CAMBs under disturbances, faults, and time delays demonstrates that the proposed control system achieves effectiveness, feasibility, and robustness.

INDEX TERMS 5-DOF conical active magnetic bearings, supply fault, time delay, fractional order control, mismatched and matched disturbances.

I. INTRODUCTION

Active magnetic bearing systems are extensively utilized in various industries. These systems employ electromagnetic

The associate editor coordinating the review of this manuscript and approving it for publication was Ladislau Matekovits.

bearings, which operate using power electronic components, to support high-speed machinery such as power drives [6], suspended flywheels [12], and turbomolecular pumps [5]. A typical active magnetic bearing system consists of four main components: an electric actuator, a digital control unit, a switching amplifier, and a position sensor. The system

²School of Electrical and Electronic Engineering, Hanoi University of Science and Technology, Hai Ba Trung, Hanoi 100000, Vietnam

³Faculty of Mechanical Engineering, Hanoi University of Civil Engineering, Hai Ba Trung, Hanoi 100000, Vietnam

⁴Automation and Control Institute, TU Wien, 1040 Vienna, Austria

⁵College of Engineering and Computer Science, VinUni, Hanoi 100000, Vietnam



includes multiple electromagnets that generate magnetic fields to suspend the rotating rotor, allowing it to levitate without physical contact. In addition, conical-shaped magnetic bearings have emerged as a promising solution for various magnetic force-supported applications due to their distinctive geometry, which reduces the number of active magnets required [21], [35], [36].

As illustrated in Fig. 1, the rotor surface at the bearing end is slightly angled, creating a slanted air gap between the rotor and the bearing. This design allows the electromagnetic coils to generate both axial and radial forces, eliminating the need for an additional set of axially controlled electromagnetic coils. The key advantages of this configuration include reduced energy consumption for supporting maximum loads and lower copper losses [22]. However, the system faces significant challenges due to high coupling effects between the axes, making the development of a reliable controller under a wide range of operating conditions a complex task [33], [37]. Studies [33] have provided a model of the conical bearing that is derived in state variable form with airgap flux, airgap displacement, and velocity being used as state variables. This description converts the equations of rotor dynamics into a simple form. However, considering the dynamics of the system, the studies ignore the variation in parametric and gyroscopic effects, which is a significant nonlinearity. A recent publication on modeling for CAMBs, where the mismatched disturbances are determined using a disturbance estimator, is presented in [35]. However, when considering the technological characteristics of the CAMBs, the above model ignores the matched disturbance effect on the control input channel. In the paper, we propose a CAMBs model that considers multi-channel lumped disturbances. The governing equations characterising the relationship between electromagnetic forces, air gaps, gyroscopic force, mass unbalance, and control currents are used to build the nonlinear model of the conical magnetic bearing. In previous studies, supply faults, power saturation under unbalanced disturbances, and unmodeled dynamics are not considered when building detailed CAMBs models. This makes the mathematical models of the objects not fully represented, especially when faults and time delays occur. Therefore, in this study, we propose to build a new, more complete model of CAMBs.

A. OVERVIEW OF CONTROL

The key point to guarantee the quality of the system output is to properly handle the saturation of coil current and lumped disturbances in CAMBs. Traditional decentralized PID control used for magnetic bearings still has some limits in exploiting the possible active potentials for controlling rotor vibration, positioning, and alignment to the fullest extent. Since a CAMBs is highly nonlinear, nonlinear control techniques are natural choices that can provide more complete consideration of the nonlinearities and inherent coupling properties and even permit greater use of available

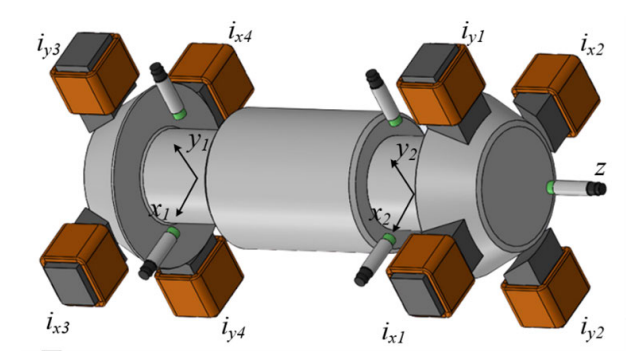


FIGURE 1. 3D visualization of the motor shaft equipped with conical active magnetic bearings.

clearance during operation. Using grey-box identification, a linear and multi-variable cone-shaped AMB system is presented in [7], and then a Linear Quadratic Regulator is used to stabilize the plant. Controllers designed using fuzzy techniques have recently been studied, and studies conducted in [18], [23], and [30] have shown that the quality and stability of the CAMBs are guaranteed, and the displacement overshoot is small. A nonlinear adaptive control is proposed in [38] to improve performance with uncertainty in the rotor angular velocity and stabilize the system over a greater range of error than the nonlinear controller without adaptation. Furthermore, sliding mode control (SMC) can effectively deal with model uncertainties and disturbances of nonlinear systems. Studies in [29], [40], and [41] indicate that the robust control method with sliding mode control for AMB has the advantages of being stable to disturbance factors and less sensitive to the variation of model parameters, especially with fast dynamic responses. Recently, SMC strategies based on the fractional-order sliding surface have been widely applied to various systems [8], [10], with good tracking performance and more robust control performance compared to traditional integer-order controllers. However, all those studies ignore the issue of current loop control, while current loop operation can have a great impact on the outer loop, especially when supply faults and time delays occur.

B. OBSERVATION

An extended state observer-based fractional-order sliding mode controller was proposed in [16], [17], and [47] to achieve rapid response, reduce tracking errors, and enhance control performance while mitigating chattering. However, the traditional ESO approach is primarily suited for systems with an Integral Chain Form structure and single-channel matched lumped disturbances [14]. In contrast, many electromagnetic systems exhibit non-ICF structures and multichannel matched and mismatched lumped disturbances [13], where the conventional ESO method becomes ineffective. Recently, generalized ESOs (GESOs) have been successfully applied to various industrial systems with non-ICF structures and mismatched lumped disturbances [39], [46]. Nonetheless, in systems experiencing multi-channel lumped



disturbances, a single GESO or ESO alone cannot reliably estimate both matched and mismatched disturbances. The limitations of traditional ESO and GESO-based control methods, as highlighted above, serve as the primary motivation for designing the Hybrid Extended State Observer (HyESO) to handle systems with multi-channel lumped disturbances.

C. OUTER LOOP

In theory, fractional-order sliding surfaces exhibit slower energy transfer during switching, leading to reduced chattering compared to integer-order sliding surfaces, which decay exponentially to zero. Experimentally, FOSMC has demonstrated superior control performance with lower chattering and greater robustness against external load disturbances and parameter variations compared to traditional integer order SMC [34]. This study integrates the disturbance compensation capability of the HyESO with the strengths of the fractional-order sliding mode control, proposing a novel HyESO-based FOSMC strategy. The key role of the HyESO is to treat modeling errors and external disturbances as the system's lumped disturbances, which are then estimated and compensated for in real time. By incorporating integral terms and fractional-order calculus into the sliding mode control, the proposed approach significantly enhances control accuracy while effectively reducing chattering in the system. The primary control command is determined by the FOSMC, while the HyESO generates a compensation control command, making the strategy suitable for both position and current control in the CAMBs.

D. INNER LOOP

Recently, the non-integer PID controller, which is also called the fractional-order PID controller, has been an emerging tool to overcome the drawbacks and limitations of conventional PID [11]. The fractional-order PID controller extends the conventional PID structure by incorporating adjustable orders for both integration and differentiation, making it a fivedegree-of-freedom controller. This added flexibility enhances system adaptability, improves dynamic response, and reduces sensitivity to disturbances. Comparative analyses between PID and FOPID have demonstrated that FOPID offers superior robustness and flexibility [43]. By tuning two additional controller parameters, i.e., the integral order and the differential order, the FOPID can outperform the traditional PID controller in drive control for motors [24], [25] and active magnetic bearing [9], [27]. For instance, an artificial intelligence-based non-integer PID controller has been designed for a control strategy for active magnetic bearing [26]. In [9], a fractional-order PID controller based on an evolutionary optimization approach for a magnetic levitation system. However, in the above studies, the issue of supply faults and time delay is still limitedly considered. Therefore, in this study, to improve the control quality under faults and time delay situations, FOPID combined with ESO is studied for the electrical system.

E. OPTIMIZATION

To enhance the control performance of active magnetic bearing systems, artificial neural networks (ANNs) can be utilized in optimization techniques. By training the neural network with specific objectives such as minimizing power consumption, reducing vibrations, or maximizing system stability, from which the control inputs can be adjusted to achieve the desired system behavior more effectively [42]. Artificial intelligence methods, including particle swarm optimization (PSO), fuzzy logic control, and ANNs, play a crucial role in improving the efficiency and reliability of AMB systems [25]. In flywheel energy storage applications, AMBs offer significant benefits, such as eliminating friction losses and maintaining performance under challenging conditions. While fuzzy logic control enables automated tuning, PSO and ANNs can optimize PID controller parameters to enhance overall system control [11]. In this study, PSO based on performance index ITAE is used for CAMBs to optimize error and energy, thereby ensuring stable operation and energy optimization for magnetic bearings, which can be applied to many operations such as flywheel.

The overall contribution of the paper is stated as follows:

- 1. *Model:* Different from basic mechanical systems of CAMBs in studies [28], [35], [36], [45], the proposed mathematical model of the 5-DOF conical magnetic bearing system that integrates both the electrical and mechanical systems under mismatched and matched disturbances is expressed. In addition, supply faults, power saturation under unbalanced disturbances, and unmodeled dynamics are considered when building detailed CAMBs models for the first time.
- 2. Theory: Distinct from studies [3], [20], [31], [35], [36], [45], [48] that only consider mismatched disturbances, ignoring supply faults, time delays, and matched disturbances. In this study, a cascaded fractional order control structure for CAMBs is proposed, comprising an outer loop and an inner loop. The outer loop employs fractional sliding mode control to regulate the rotor's displacement and rotational angle. Meanwhile, the inner loop utilizes a fractional-order PID controller to control coil currents, effectively mitigating the time delay issues associated with power supplies and sensors. Matched and mismatched disturbances are addressed through a hybrid extended state observer structure, where a fast ESO is implemented in the inner loop, while a slow ESO is applied to the outer loop to observe mismatched and matched disturbances.
- 3. Evaluation method: PSO using performance index ITAE is proposed for CAMBs to tune the parameters of both the inner loop and outer loop to optimize the energy consumption and errors of the controllers and observers, including fractional order parameters.

The remainder of this study is organized as follows: An introduction to the CAMBs with multi-channel lumped disturbances is detailed in Section II. In Section III, the hybrid ESO strategy is proposed to deal with the problem of the mismatched and matched disturbances. Fractional order controllers, including FOPID and FOSMC, are analyzed in



Section IV. Simulations are shown in Section V, including a comparison between the controllers of the inner loop and the outer loop. Finally, the main conclusions of this study are drawn in Section VI.

II. SYSTEM DESCRIPTION AND MATHEMATICAL MODEL

A. MECHANICAL SYSTEM

1) PROBLEM SETTING

Assuming that, the rotational motion of the rotor arounded z-axis are independently controlled by the motor in speed control mode. Thus, the motions of the CAMBs are included the translational and rotational motions of the rotor along x, y- axes. Then, the CAMBs includes five degrees of freedom as shown in Figs. 1-2.

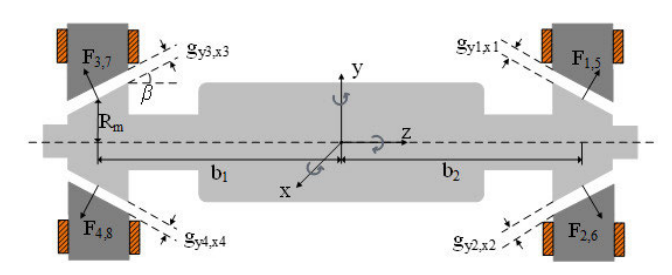


FIGURE 2. Schematic of conical active magnetic bearing forces.

The mechanical diagram for the rotor-bearing system is illustrated in Fig. 2. Assuming that the rotor is rigid, then the second-order equations of motion for the rotor can be represented as usual by using the Newton-Euler law of motion:

$$m\ddot{z} = (F_1 + F_2 + F_5 + F_6)\sin\beta$$

$$- (F_3 + F_4 + F_7 + F_8)\sin\beta + F_z$$

$$m\ddot{x} = (F_5 - F_6 + F_7 - F_8)\cos\beta + F_x$$

$$m\ddot{y} = (F_1 - F_2 + F_3 - F_4)\cos\beta - mg + F_y$$

$$J_d\ddot{\theta}_x + J_p\dot{\theta}_y\Omega = [(F_1 - F_2)b_2 + (F_4 - F_3)b_1]\cos\beta$$

$$+ (F_2 - F_1 + F_3 - F_4)R_m\sin\beta + M_x$$

$$J_d\ddot{\theta}_y - J_p\dot{\theta}_x\Omega = [(F_6 - F_5)b_2 + (F_7 - F_8)b_1]\cos\beta$$

$$+ (F_5 - F_6 + F_8 - F_7)R_m\sin\beta + M_y$$
(1)

where z, y, and x represent the three radial translations, while θ_x and θ_y denote rotations about the x-axis and y-axis, respectively. The parameter m represents the rotor mass, J_d and J_p are the transverse and polar moments of inertia of the rotor, respectively, and Ω is the rotor's rotational speed. F_j (j=1 to 8) denotes the forces at the bearings, whereas F_x , F_y , M_x , and M_y represent external disturbances acting on the rotor. The parameters b_1 and b_2 define the bearing span, R_m is the effective radius, and β is the inclination angle.

In the two rotational kinematics equations, a gyroscopic effect, which is a significant nonlinearity associated with the rotor dynamics is considered. The gyroscopic effect in the CAMBs induces coupling between the pitch motion (rotation about the x-axis) and yaw motion (rotation about

the y-axis), with its intensity increasing proportionally to the rotor's rotational speed. This phenomenon significantly complicates the stabilization of the system, particularly in high-speed applications. Nomenclature of CAMBs is summarized in Table 1.

TABLE 1. Parameters of CAMBs.

Symbol	Name	Value	Unit
Parameters of mechanical system			
g_0	Nominal air gap	0.45	mm
m	Rotor mass	0.755	kg
J_p	Polar moment of inertia	$1.54 \cdot 10^{-4}$	kg m ²
J_d	Diametral moment of inertia	$31.68 \cdot 10^{-4}$	kg m ²
β	Magnetic core inclined angle	0.98	rad
b_1	Distance between bearing (1) and COG	55	mm
b_2	Distance between bearing (2) and COG	55	mm
R_m	Effective radius	12.4	mm
Parameters of electrical system			
N_t	Coil turns	82	-
$R_{\rm coil}$	Coil resistance	0.5	Ω
L_0	Nominal inductance	1.2	mH
S	Pole cross-sectional area	118	mm^2

2) LINEARIZED BEARING FORCE MODEL

Assuming the reluctance of the iron is neglected concerning the gap reluctance. In addition, all magnets have an identical structure, and the fringing effect can be neglected; the electromagnetic forces are given as follows [36]:

$$F_k = \frac{\mu_0 N^2 A_p}{4} \frac{i_{yk}^2}{g_{yk}^2}; \quad k = 1, \dots, 4$$

$$F_j = \frac{\mu_0 N^2 A_p}{4} \frac{i_{xm}^2}{g_{xm}^2}; \quad j = 5, \dots, 8$$
 (2)

where m=j-4; $\mu_0=4\pi\times 10^{-7} \text{H/m}$ is the air permeability. Equation (2) shows that the force for an active magnetic bearing is proportional to the square of the current and inversely ratio to the displacement. This quadratic relationship is inconvenient for control purposes, it is much more desirable to have a linear relation between the control current and force. The bearing air gaps presented in (3) can be referred to the center of gravity (COG) coordinates involving the geometrical quantities introduced in Fig. 2 as follows:

$$g_{1,2} = g_o - z \sin \beta \mp (y + b_2 \theta_x) \cos \beta$$

$$g_{3,4} = g_o + z \sin \beta \mp (y - b_1 \theta_x) \cos \beta$$

$$g_{5,6} = g_o - z \sin \beta \mp (x - b_2 \theta_y) \cos \beta$$

$$g_{7,8} = g_o + z \sin \beta \mp (x + b_1 \theta_y) \cos \beta$$
(3)

The coil current of the system can be calculated through the control strategy "differential driving mode". The general principle is that one electromagnet is driven with the sum of a bias and a control current, while the opposite one with their difference. Five control currents \mathbf{i}_r are used to control the five-DOF plant. The currents flowing along the coils are expressed as follows:

$$\mathbf{i} = \mathbf{I}_0 + \mathbf{H}\mathbf{I}_r \tag{4}$$



The details of (4) are provided in the appendix. By applying (3) and (4) to (2) and (1), and utilizing the Taylor series expansion, the magnetic force is linearized as follows:

$$\mathbf{F}_{amb} = -\mathbf{K}_d \mathbf{q} + \mathbf{K}_i \mathbf{i} \tag{5}$$

where $\mathbf{q} = \begin{bmatrix} z \ x \ y \ \theta_x \ \theta_y \end{bmatrix}^T$ denote states of CAMBs; \mathbf{K}_d is stiffness matrix of the CAMBs and \mathbf{K}_i is stiffness current matrix. The linear magnetic field is assumed above, however in practice there exists hysteresis and saturation in the magnetic field so that the magnetic field is not linear. Hence, the exists uncertainties are called unmodeled magnetic force, including fringing effect, flux leakage, and high-order components are omitted in the Taylor expansion.

3) UNBALANCE DISTURBANCES

Rotor mass unbalance of magnetically levitated rotors causes deterioration of dynamic and static characteristics. The eccentricity of the rotor causes unbalanced vibration, which is a common problem in rotating machinery. When the rotor is compelled to rotate around its center of inertia, G_m , rather than its geometric center, G, a centrifugal force arises due to the acceleration of the inertia center. This force generates a synchronous transmitted force, leading to synchronous rotor displacement. In extreme cases, as the imbalance effect increases with the rotor's rotational speed, high-speed operation can cause the rotor to whirl beyond the permissible air gap. This may lead to partial or even full annular contact with the stator, potentially causing irreversible damage to the bearing system.

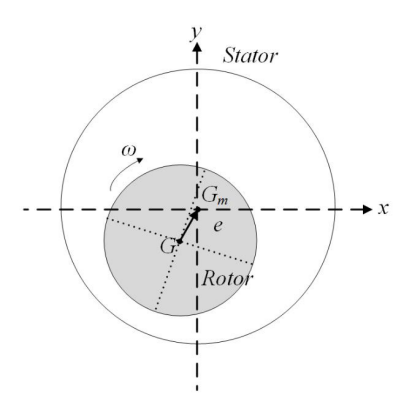


FIGURE 3. Illustration of unbalanced rotor.

The unbalance is modelled as a residual mass displaced from the rotating axis, which is combined into one variable called unbalance moment me_{unb} , and the phase is θ_{unb} . The static and dynamic imbalances, which are presented as follows:

$$\mathbf{F}_{unb} = \begin{bmatrix} F_z \\ F_x \\ F_y \\ T_x \\ T_y \end{bmatrix} = \begin{bmatrix} 0 \\ me\omega^2 \cos(\omega t + \theta) \\ me\omega^2 \sin(\omega t + \theta) \\ (J_d - J_p) \varepsilon\omega^2 \cos(\omega t + \theta) \\ (J_d - J_p) \varepsilon\omega^2 \sin(\omega t + \theta) \end{bmatrix}$$
(6)

 θ is the initial phase of the mass center, e is eccentricity and ϵ is inclination angle.

Remark 1: Based on the analysis of Fig. 3 and the dynamic imbalances (6), the faster the rotor rotates, the larger the amplitude and frequency of the unbalanced disturbances. This type of active magnetic bearing drive is specially designed to operate at very high speeds. Therefore, it is necessary to build a high-precision controller so that when external disturbances impact the rotor, the impact can be minimized, ensuring stable operation of the CAMBs.

B. ELECTRICAL SYSTEM UNDER SUPPLY FAULT

1) IDEAL MODEL

As shown in Fig. 1, CAMBs needs to use 8 electromagnets for contactless lifting control for the rotor section. The prototype structure of the electromagnet is illustrated as in Fig. 4.

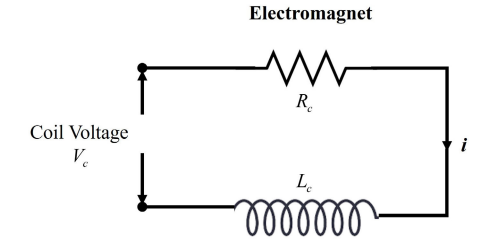


FIGURE 4. Prototype structure of electromagnet.

The coil voltage V_c given in Fig. 4 across the electromagnet's coil from Kirchhoff's law is given as follows:

$$\mathbf{V}_c = \mathbf{L}_c \frac{d\mathbf{i}}{dt} + \mathbf{R}_c \mathbf{i} \tag{7}$$

where \mathbf{L}_c is the coil inductance, \mathbf{R}_c is coil resistance.

2) UNCERTAINTY MODEL

The uncertainty parameter model combines the uncertainty of the coil inductance (\mathbf{L}_c) and the coil resistance (\mathbf{R}_c). The effect of uncertainty parameters and external disturbances is called a matched disturbance. Equation (7) can be rewritten under the matched disturbances as follows:

$$\mathbf{L}_{c}\frac{d\mathbf{i}}{dt} = \mathbf{V}_{c} - \mathbf{R}_{c}\mathbf{i} + \mathbf{L}_{m}$$
 (8)

where $\mathbf{L}_m = -\Delta \mathbf{L}_c \frac{d\mathbf{i}}{dt} - \Delta \mathbf{R_c} \mathbf{i} + \Delta \mathbf{L}_m$ is the matched lumped disturbance influenced by unmodeled dynamic such as eddy currents $\Delta \mathbf{L}_m$.

3) FAULT AND SATURATION SUPPLY MODEL

The fault and saturation supply model of each electromagnet coil is described as follows:

$$V_{c}(t) = V_{c0}(t) + ((\rho(t) - 1) \operatorname{sat}(V_{c0}(t)) + V_{cf}(t) + \Delta V_{c0})$$
(9)

where V_{c0} and V_c represent the desired control input and the actual control input, respectively. ΔV_{c0} denotes the difference between the desired control input and the actual control input. $\rho(t)$ denotes an effectiveness indicator satisfying



 $0 \le \rho(t) \le 1$. $V_{cf}(t)$ denotes the unknown additive supply fault that is time-varying, immeasurable, and completely out of control.

In (9), four fault conditions need to be considered as follows:

- 1) **Healthy condition:** For $\rho = 1$ and $V_{cf} = 0$, the power supply operates normally.
- 2) Bias fault condition: For $\rho = 1$ and $V_{cf} \neq 0$, the power supply experiences an additive fault.
- 3) **Partial loss of effectiveness condition:** For $0 < \rho < 1$ and $V_{cf} = 0$, the power supply suffers from partial power loss but remains operational.
- 4) **Stuck fault condition:** For $\rho = 0$ and $V_{cf} \neq 0$, the power supply encounters a stuck fault. The stuck fault condition typically occurs when the number of supply powers exceeds the number of control outputs, necessitating further investigation of control allocation schemes.

In this study, both loss of effectiveness and bias faults are concurrently considered for the electrical system of CAMBs. To address this problem, the fast ESO is used to estimate the lumped disturbances that include fault and saturation supplies.

4) TIME DELAY

When both input time delay and sensor delay coexist in a system, their effects add up and can cause serious performance degradation. In this study, the input time delay and sensor delay of the electrical system are considered as pure time delay. From which the first order transfer function of the electrical system with a time delay is given as follows:

$$G(s) = \frac{1}{R_c + L_c s} e^{-s\tau} \tag{10}$$

where τ is the time constant of the system, including time constant of sensors and the time constant of supply powers.

Remark 2: The time delay problem of supplying power and sensors will greatly affect the control quality of the system. To solve the above problem, fractional order PID is studied and applied to the electrical system of CAMBs, thereby improving the control quality compared to the conventional PID. The detailed comparison between PID and FOPID will be presented in scenario 1 in the numerical simulation study.

C. COMBINED MODEL

AMBs are a group of nonlinear and unstable dynamical systems with multi-channel matched and mismatched kind of lumped disturbances [15], [32]. The model of mismatched lumped disturbance combined the effects of external disturbance, the uncertain electromagnetic force, and parametric uncertainties. The parametric uncertainties come from manufacturing and assembly errors in the nominal air gap g_0 , inclined angle β , rotor mass m, or the other parameters of the rotor of CAMBs. Combining (1), (5), and (6) we

obtain:

$$M\ddot{\mathbf{q}} + \mathbf{G}\dot{\mathbf{q}} + \mathbf{K}_d\mathbf{q} = \mathbf{K}_i\mathbf{i} + \mathbf{F}_{unb} \tag{11}$$

Considering the parametric uncertainties in (11) we have

$$\mathbf{M}\ddot{\mathbf{q}} = \mathbf{K}_i \mathbf{i} + \mathbf{L}_{mm} \tag{12}$$

where $\mathbf{L}_{mm} = -\Delta \mathbf{M}\ddot{\mathbf{q}} - (\mathbf{G} + \Delta \mathbf{G})\dot{\mathbf{q}} - (\mathbf{K}_d + \Delta \mathbf{K}_d)\mathbf{q} + \Delta \mathbf{K}_i\mathbf{i} + \mathbf{F}_{unb}$ is mismatched lumped disturbance. Using above differential equations, nonlinear state space model for the rotor of CAMBs is developed by rotor position, rotor velocity and coil current as three state variables as $\mathbf{x}_1 = \mathbf{q}$; $\mathbf{x}_2 = \dot{\mathbf{q}}$; $\mathbf{x}_3 = \mathbf{i}$ and coil voltage (\mathbf{V}_c) as controlled input (\mathbf{u}) with rotor displacement \mathbf{q} as output variable.

$$\begin{cases} \dot{\mathbf{x}}_1 = \mathbf{x}_2 \\ \dot{\mathbf{x}}_2 = \mathbf{M}^- \mathbf{K}_i \mathbf{x}_3 + \mathbf{M}^- \mathbf{L}_{mm} \\ \dot{\mathbf{x}}_3 = \mathbf{L}_c^- \mathbf{u} - \mathbf{L}_c^- \mathbf{R}_c \mathbf{i} + \mathbf{L}_c^- \mathbf{L}_m \end{cases}$$
(13)

The lumped disturbances of CAMBs include uncertainty parameters, unmodeled dynamics, unbalanced rotors, unknown disturbances, force coefficients, actual air gaps on the plant, and system geometry, among others.

Assumption 1: Since the energy within an integral system is inherently constrained in physical applications, the uncertainties present in the system remain bounded. They typically depend on factors such as rotor position, coil currents, and other physical parameters, which do not undergo abrupt changes. Suppose that the amplitudes of the mismatch disturbances \mathbf{L}_{mm} and matched disturbances \mathbf{L}_m and it's derivative are bounded variation.

III. HYBRID EXTENDED STATE OBSERVER

The ESO technique is primarily suited for systems with an integral chain form structure and single-channel lumped disturbances that are matched. However, in many control applications, systems often exhibit non-ICF structures and involve multi-channel lumped disturbances, both matched and mismatched, where the conventional ESO approach may not be effective. To address this limitation, a hybrid extended state observer scheme has been developed to estimate and compensate for both matched and mismatched lumped disturbances.

The hybrid extended state observer is defined as follows: Mismatched dynamics:

$$\begin{cases} \dot{\hat{\mathbf{x}}}_{1} = \hat{\mathbf{x}}_{2} + \beta_{1} \left(\mathbf{x}_{1} - \hat{\mathbf{x}}_{1} \right) \\ \dot{\hat{\mathbf{x}}}_{2} = \varphi_{1} + \hat{\mathbf{x}}_{e1} + \beta_{2} \left(\mathbf{x}_{1} - \hat{\mathbf{x}}_{1} \right) \\ \dot{\hat{\mathbf{x}}}_{e1} = \beta_{3} \left(\mathbf{x}_{1} - \hat{\mathbf{x}}_{1} \right) \end{cases}$$
(14)

where

$$\begin{aligned} \varphi_1 &= \mathbf{M}^- \mathbf{K}_i \mathbf{x}_3 \\ \beta_1 &= \left[3\omega_1; 3\omega_1; 3\omega_1; 3\omega_1; 3\omega_1 \right] \\ \beta_2 &= \left[3\omega_1^2; 3\omega_1^2; 3\omega_1^2; 3\omega_1^2; 3\omega_1^2 \right] \\ \beta_3 &= \left[\omega_1^3; \omega_1^3; \omega_1^3; \omega_1^3; \omega_1^3 \right] \end{aligned}$$

IEEE Access

Matched dynamics:

$$\begin{cases} \dot{\hat{\mathbf{x}}}_3 = \varphi_2 + \hat{\mathbf{x}}_{e2} + \theta_1 \left(\mathbf{x}_3 - \hat{\mathbf{x}}_3 \right) \\ \dot{\hat{\mathbf{x}}}_{e2} = \theta_2 \left(\mathbf{x}_3 - \hat{\mathbf{x}}_3 \right) \end{cases}$$
(15)

where $\varphi_2 = \mathbf{L}_c^- \mathbf{u} - \mathbf{L}_c^- \mathbf{R}_c \mathbf{i}$ $\theta_1 = \begin{bmatrix} 2\omega_2; 2\omega_2; 2\omega_2; 2\omega_2; 2\omega_2; 2\omega_2; 2\omega_2; 2\omega_2 \end{bmatrix} \theta_2 = \begin{bmatrix} \omega_2^2; \omega_2^2; \omega_2^2; \omega_2^2; \omega_2^2; \omega_2^2; \omega_2^2; \omega_2^2; \omega_2^2; \omega_2^2 \end{bmatrix}$ and ω_1 , ω_2 denotes positive observer gains to be determined. The estimation errors are defined as follows:

$$\begin{cases} \dot{\tilde{\mathbf{x}}}_{1} = \tilde{\mathbf{x}}_{2} - \beta_{1}\tilde{\mathbf{x}}_{1} \\ \dot{\tilde{\mathbf{x}}}_{2} = \tilde{\varphi}_{1} + \tilde{\mathbf{x}}_{e1} - \beta_{2}\tilde{\mathbf{x}}_{1} \\ \dot{\tilde{\mathbf{x}}}_{e1} = -\beta_{3}\tilde{\mathbf{x}}_{1} \end{cases}$$

$$\begin{cases} \dot{\tilde{\mathbf{x}}}_{3} = \tilde{\varphi}_{2} + \tilde{\mathbf{x}}_{e2} - \theta_{1}\tilde{\mathbf{x}}_{3} \\ \dot{\tilde{\mathbf{x}}}_{e2} = -\theta_{2}\tilde{\mathbf{x}}_{3} \end{cases}$$

$$(16)$$

To facilitate the stability analysis, the scaled estimation errors are defined as $\varepsilon = \begin{bmatrix} \varepsilon_1 & \varepsilon_2 & \varepsilon_3 \end{bmatrix}^T = \begin{bmatrix} \tilde{\mathbf{x}}_1 & \tilde{\mathbf{x}}_2/\omega_1 & \tilde{\mathbf{x}}_{e1}/\omega_1^2 \end{bmatrix}^T$ and $v = \begin{bmatrix} v_1 & v_2 \end{bmatrix}^T = \begin{bmatrix} \tilde{\mathbf{x}}_3 & \tilde{\mathbf{x}}_{e2}/\omega_2 \end{bmatrix}^T$ and the dynamics (16) can

$$\dot{\varepsilon} = \omega_1 \mathbf{A}_1 \varepsilon + \mathbf{B}_1 \frac{\tilde{\varphi}_1}{\omega_1} + \mathbf{B}_2 \frac{\delta_1}{\omega_1^2}$$

$$\dot{v} = \omega_2 \mathbf{A}_2 v + \mathbf{B}_3 \frac{\tilde{\varphi}_2}{\omega_2} + \mathbf{B}_4 \frac{\delta_2}{\omega_2^2}$$
(17)

where

$$\mathbf{A}_{1} = \begin{bmatrix} -3 & 1 & 0 \\ -3 & 0 & 1 \\ -1 & 0 & 0 \end{bmatrix}, \quad \mathbf{B}_{1} = \begin{bmatrix} 0 \\ 1 \\ 0 \end{bmatrix}, \quad \mathbf{B}_{2} = \begin{bmatrix} 0 \\ 0 \\ 1 \end{bmatrix}$$
$$\mathbf{A}_{2} = \begin{bmatrix} -2 & 1 \\ -1 & 0 \end{bmatrix}, \quad \mathbf{B}_{3} = \begin{bmatrix} 1 \\ 0 \end{bmatrix}, \quad \mathbf{B}_{4} = \begin{bmatrix} 0 \\ 1 \end{bmatrix}$$

The A_1 and A_2 are Hurwitz matrix, thus, there are positive define matrices P_1 and P_2 satisfying these functions where I denotes an identify matrix $\mathbf{A}_1^T \mathbf{P}_1 + \mathbf{P}_1 \mathbf{A}_1 = -\mathbf{I}$ and $\mathbf{A}_2^T \mathbf{P}_2 +$ $\mathbf{P}_2 \mathbf{A}_2 = -\mathbf{I}$. A Lyapunov function V_1 is defined as

$$V_1 = \frac{1}{2} \left(\varepsilon^T \mathbf{P}_1 \varepsilon + \nu^T \mathbf{P}_2 \nu \right) \tag{18}$$

The derivative of V_1 can be deduced as

$$\dot{V}_{1} = \frac{1}{2} \left(\dot{\varepsilon}^{T} \mathbf{P}_{1} \varepsilon + \varepsilon^{T} \mathbf{P}_{1} \dot{\varepsilon} + \dot{v}^{T} \mathbf{P}_{2} v + v^{T} \mathbf{P}_{2} \dot{v} \right)
= \frac{1}{2} \omega_{1} \varepsilon^{T} \left(\mathbf{A}_{1}^{T} \mathbf{P}_{1} + \mathbf{P}_{1} \mathbf{A}_{1} \right) \varepsilon + \frac{1}{2} \omega_{1} v^{T}
\times \left(\mathbf{A}_{2}^{T} \mathbf{P}_{2} + \mathbf{P}_{2} \mathbf{A}_{2} \right) v + \varepsilon^{T} \left(\mathbf{P}_{1} \mathbf{B}_{1} \frac{\tilde{\varphi}_{1}}{\omega_{1}} + \mathbf{P}_{1} \mathbf{B}_{2} \frac{\delta_{1}}{\omega_{1}^{2}} \right)
+ v^{T} \times \left(\mathbf{P}_{2} \mathbf{B}_{3} \frac{\tilde{\varphi}_{2}}{\omega_{2}} + \mathbf{P}_{2} \mathbf{B}_{4} \frac{\delta_{2}}{\omega_{2}^{2}} \right)
= -\frac{1}{2} \omega_{1} \varepsilon^{T} \varepsilon - \frac{1}{2} \omega_{2} v^{T} v + \varepsilon^{T} \Xi_{1} + v^{T} \Xi_{2} \tag{19}$$

According to the inequality theorem, the boundness of the above function can be obtained by

$$\dot{V}_1 \le -\frac{1}{2}\omega_1 \varepsilon^T \varepsilon - \frac{1}{2}\omega_2 v^T v + \frac{1}{2}\varepsilon^T \varepsilon$$

$$+ \frac{1}{2}\Xi_{1}^{T}\Xi_{1} + \frac{1}{2}\nu^{T}\nu + \frac{1}{2}\Xi_{2}^{T}\Xi_{2}$$

$$= -\frac{1}{2}(\omega_{1} - 1)\varepsilon^{T}\varepsilon - \frac{1}{2}(\omega_{2} - 1)\nu^{T}\nu$$

$$+ \frac{1}{2}\Xi_{1}^{T}\Xi_{1} + \frac{1}{2}\Xi_{2}^{T}\Xi_{2}$$

$$\leq -\frac{1}{2}\omega_{\min}\left(\varepsilon^{T}\varepsilon + \nu^{T}\nu\right) + \chi_{0}$$
(20)

where $\omega_{\min} = \min \{ \omega_1 - 1, \omega_2 - 1 \}$ It is evident that $\dot{V}_1 \le$ 0 if the observer gains ω_1 and ω_2 are selected satisfying $\omega_1 > 1$, $\omega_{\min} (\varepsilon^T \varepsilon + v^T v) > 2\chi_0$. Thus, the estimation errors ε and ν are bounded, suggesting that $\tilde{\mathbf{x}}_i$ and $\tilde{\mathbf{x}}_{ei}$ are ultimately bounded. The aforementioned HyESO estimates the whole system states, including the unmeasurable velocity and total disturbance. The estimated states will be adopted in the following controller design.

IV. FRACTIONAL ORDER CONTROL SYSTEM

A. OUTER LOOP

1) FRACTIONAL CALCULUS

Fractional calculus has existed since the inception of integerorder calculus, though it was traditionally regarded as a purely mathematical concept. However, in recent decades, it has gained significant attention in system analysis and control engineering. The fractional-order fundamental operator, denoted as $t_0 D_t^{\alpha}$, is defined as follows [19]:

$$D^{\alpha} \triangleq {}_{t_0}D_t^{\alpha} = \begin{cases} \frac{d^{\alpha}}{dt^{\alpha}}, & R(\alpha) > 0, \\ 1, & R(\alpha) = 0, \\ \int_{t_0}^t (d\tau)^{-\alpha}, & R(\alpha) < 0. \end{cases}$$
 (21)

where t_0 and t are the limits of the operation, α is the order of the operation, and generally $\alpha \in R$ and α can be a complex number. The two most commonly used definitions for the general fractional differentiation and integration are the Caputo-Fabrizio definition, the Grunwald-Letnikov definition, and the Riemann-Liouville definition. The fractional differential of Caputo-Fabrizio is defined as [44]:

$${}_{t_0}^C D_t^{\alpha} f(t) = \frac{1}{\Gamma(n-\alpha)} \int_{t_0}^t \frac{f^{(n)}(\tau)}{(t-\tau)^{\alpha-n+1}} d\tau$$
 (22)

where $\alpha \geq 0$ and $n-1 \leq \alpha < n$, n is a positive integer, $\Gamma(\cdot)$ is the Gamma function. The fractional differential of Riemann-Liouville is defined as follows [44]:

$${}_{a}^{RL}D_{t}^{\alpha}f(t) = \frac{1}{\Gamma(n-\alpha)} \left(\frac{d}{dt}\right)^{n} \int_{t_{0}}^{t} \frac{f(\tau)}{(t-\tau)^{1-(n-\alpha)}} d(\tau)$$
 (23)

Under the zero initial condition, the Laplace transform of fractional calculus is defined as follows [19]:

$$L\left\{t_0 D_t^{\alpha} f\left(t\right)\right\} = s^{\alpha} F\left(s\right) \tag{24}$$

Remark 3: These fractional order derivative definitions (23) and (24) have several advantages, but they are



not suitable for all cases. On the one hand, in the Riemann-Liouville type, when the fractional differential equations are used to describe real-world processes, the Riemann-Liouville derivative has some drawbacks. Thus, the applicability range of Riemann-Liouville fractional derivatives is limited [1]. For differentiability, the Caputo derivative requires higher regularity conditions: to calculate the fractional derivative of a function in the Caputo type, we should first obtain its derivative. Caputo derivatives are defined only for differentiable functions, while the functions that do not have a first-order derivative may have fractional derivatives of all orders less than one in the Riemann-Liouville sense [4].

2) FRACTIONAL SLIDING MODE CONTROLLER

In this study, the fractional order sliding mode controller for the state control of CAMBs is proposed to improve the robustness and effectiveness of the control system. Defining the state error as follows:

$$\mathbf{e} = \mathbf{q} - \mathbf{r} = \mathbf{x}_1 - \mathbf{r} \tag{25}$$

where \mathbf{r} is the reference input. The dynamic of error \mathbf{e} is given as:

$$\dot{\mathbf{e}} = \mathbf{x}_2 - \dot{\mathbf{r}} \tag{26}$$

when defining $\mathbf{v} = \mathbf{M}^{-}\mathbf{K}_{i}\mathbf{x}_{3}$, we have:

$$\ddot{\mathbf{e}} = \dot{\mathbf{x}}_2 - \ddot{\mathbf{r}} = (\mathbf{v} + \mathbf{x}_{e1}) - \ddot{\mathbf{r}} \tag{27}$$

According to the theory of fractional order calculus, a fractional order sliding surface is defined as follows:

$$\mathbf{s} = \mathbf{c}_1 \mathbf{e} + \dot{\mathbf{e}} + \mathbf{c}_2 D^{-\alpha} \mathbf{e} \tag{28}$$

where c_1 , c_2 are controller parameters and $\alpha \in (0, 1]$ is the fractional order. The system dynamics along the sliding surface is given as follows:

$$\dot{\mathbf{s}} = \mathbf{c}_1 \dot{\mathbf{e}} + \ddot{\mathbf{e}} + \mathbf{c}_2 D^{1-\alpha} \mathbf{e}$$

$$= \mathbf{c}_1 (\mathbf{x}_2 - \dot{\mathbf{r}}) + (\mathbf{v} + \mathbf{x}_{e1}) - \ddot{\mathbf{r}}$$

$$+ \mathbf{c}_2 D^{1-\alpha} (\mathbf{x}_1 - \mathbf{r})$$
(29)

Moreover, the observed sliding mode variable is $\hat{\mathbf{s}} = \mathbf{c}_1 \hat{\mathbf{e}} + \hat{\mathbf{e}} + \mathbf{c}_2 D^{-\alpha} \hat{\mathbf{e}}$, where $\hat{\mathbf{e}} = \hat{\mathbf{x}}_1 - \mathbf{r}$, $\hat{\mathbf{e}} = \hat{\mathbf{x}}_2 - \dot{\mathbf{r}}$. Choosing the fractional order SMC law as follows:

$$\mathbf{v} = \ddot{\mathbf{r}} - \mathbf{c}_1 \left(\hat{\mathbf{x}}_2 - \dot{\mathbf{r}} \right) - \hat{\mathbf{x}}_{e1} - \mathbf{c}_2 D^{1-\alpha} \left(\hat{\mathbf{x}}_1 - \mathbf{r} \right) - \eta \operatorname{sgn} \left(\hat{\mathbf{s}} \right)$$
(30)

where $\eta > 0$. By using $\mathbf{v} = \mathbf{M}^{-}\mathbf{K}_{i}\mathbf{x}_{3}$ the current reference is calculated as follows:

$$\mathbf{I}_{ref} = \mathbf{K}_i^{-1} \mathbf{M} \mathbf{v} \tag{31}$$

where \mathbf{I}_{ref} is the reference signal of inner loop. In order to achieve the highly precise tracking control and low chattering value, the sign function should be replaced by a saturation function.

3) STABILITY ANALYSIS

In the case of a fully actuated system with full state feedback, it has been established that the sliding control method guarantees that the system response reaches the sliding surface and that the surface is asymptotically stable. Defining a candidate Lyapunov function as follows:

$$V = \frac{1}{2}\mathbf{s}^T\mathbf{s} \tag{32}$$

Asymptotic stability of the system under uncertainties is guaranteed as the derivative of the Lyapunov function is negative definite. Differentiating (32) with respect to time, the following equation is obtained as follows:

$$\dot{V} = \mathbf{s}^T \dot{\mathbf{s}} \tag{33}$$

Substituting (28) and (29) into (33), we can obtain as follows:

$$\dot{V} = \mathbf{s}^T \left(\mathbf{c}_1(\mathbf{x}_2 - \dot{\mathbf{r}}) + (\mathbf{v} + \mathbf{x}_{e1}) - \ddot{\mathbf{r}} + \mathbf{c}_2 D^{1-\alpha} \right)$$

$$\times (\mathbf{x}_1 - \mathbf{r})$$
(34)

Now putting the value of control input from (30) and (31), (34) becomes:

$$\dot{V} = \mathbf{s}^{T} (\mathbf{c}_{1}(\mathbf{x}_{2} - \dot{\mathbf{r}}) + (\ddot{\mathbf{r}} - \mathbf{c}_{1}(\hat{\mathbf{x}}_{2} - \dot{\mathbf{r}}) - \hat{\mathbf{x}}_{e1} - \mathbf{c}_{2}D^{1-\alpha} \\
(\hat{\mathbf{x}}_{1} - \mathbf{r}) - \eta \operatorname{sgn}(\hat{\mathbf{s}}) + \mathbf{c}_{2}D^{1-\alpha}(\mathbf{x}_{1} - \mathbf{r}) + \mathbf{x}_{e1} - \ddot{\mathbf{r}}) \\
+ \psi \dot{\mathbf{i}}_{r} - \mathbf{x}_{e2})) \\
= \mathbf{s}^{T} (-\eta \operatorname{sgn}(\hat{\mathbf{s}}) + (\mathbf{x}_{e1} - \hat{\mathbf{x}}_{e1}) + \mathbf{c}_{1}(\mathbf{x}_{2} - \hat{\mathbf{x}}_{2} + \mathbf{c}_{2} \\
\times D^{1-\alpha}(\mathbf{x}_{1} - \hat{\mathbf{x}}_{1})) \\
= (\hat{\mathbf{s}} + \mathbf{s}^{T} - \hat{\mathbf{s}})\eta \operatorname{sgn}(\hat{\mathbf{s}}) + (\hat{\mathbf{s}} + \mathbf{s}^{T} - \hat{\mathbf{s}})(\mathbf{x}_{e1} - \hat{\mathbf{x}}_{e1}) \\
(\hat{\mathbf{s}} + \mathbf{s}^{T} - \hat{\mathbf{s}})\sigma_{1}(\mathbf{x}_{2} - \hat{\mathbf{x}}_{2}) + (\hat{\mathbf{s}} + \mathbf{s}^{T} - \hat{\mathbf{s}})\mathbf{c}_{2}D^{1-\alpha} \\
\times (\mathbf{x}_{1} - \hat{\mathbf{x}}_{1}) \\
(\hat{\mathbf{s}} + \mathbf{s}^{T} - \hat{\mathbf{s}})\sigma_{1}(\mathbf{x}_{2} - \hat{\mathbf{x}}_{2}) + (\hat{\mathbf{s}} + \mathbf{s}^{T} - \hat{\mathbf{s}})\sigma_{2}D^{1-\alpha} \\
\times (\mathbf{x}_{1} - \hat{\mathbf{x}}_{1}) \\
\dot{V} \leq -\hat{\mathbf{s}}\eta \operatorname{sgn}(\hat{\mathbf{s}}) + (|(\mathbf{x}_{e1} - \hat{\mathbf{x}}_{e1})| + c|(\mathbf{x}_{2} - \hat{\mathbf{x}}_{2})| + \mathbf{c}_{2} \\
\times D^{1-\alpha}|(\mathbf{x}_{1} - \hat{\mathbf{x}}_{1})|) \hat{\mathbf{s}} + |\mathbf{s}^{T} - \hat{\mathbf{s}}|(|(\mathbf{x}_{e1} - \hat{\mathbf{x}}_{e1})| + \mathbf{c}_{2} \\
\times D^{1-\alpha}|(\mathbf{x}_{1} - \hat{\mathbf{x}}_{1})|) + \sigma_{1}|(\mathbf{x}_{1} - \hat{\mathbf{x}}_{1})|) + \eta |\mathbf{s}^{T} - \hat{\mathbf{s}}| \\
= -\eta |\hat{\mathbf{s}}| + \eta |\mathbf{s}^{T} - \mathbf{s}| + (|(\mathbf{x}_{e1} - \hat{\mathbf{x}}_{e1})| + c|(\mathbf{x}_{2} - \hat{\mathbf{x}}_{2})| \\
+ \mathbf{c}_{2}D^{1-\alpha}|(\mathbf{x}_{1} - \hat{\mathbf{x}}_{1})|) \hat{\mathbf{s}} \hat{\mathbf{s}}^{T} - \hat{\mathbf{s}}|(|(\mathbf{x}_{e1} - \hat{\mathbf{x}}_{e1})| + c \\
\times |(\mathbf{x}_{2} - \hat{\mathbf{x}}_{2})| + \mathbf{c}_{2}D^{1-\alpha}|(\mathbf{x}_{1} - \hat{\mathbf{x}}_{1})|)$$
(36)

Because of the convergence of the extended state observer,

$$\eta \left| \mathbf{s}^{T} - \hat{\mathbf{s}} \right| + \left(\left| \left(\mathbf{x}_{e1} - \hat{\mathbf{x}}_{e1} \right) \right| + c \left| \left(\mathbf{x}_{2} - \hat{\mathbf{x}}_{2} \right) \right| + \mathbf{c}_{2} D^{1-\alpha} \\
\times \left| \left(\mathbf{x}_{1} - \hat{\mathbf{x}}_{1} \right) \right| \right) \hat{\mathbf{s}} + \left| \mathbf{s}^{T} - \hat{\mathbf{s}} \right| \left(\left| \left(\mathbf{x}_{e1} - \hat{\mathbf{x}}_{e1} \right) \right| + c \left| \left(\mathbf{x}_{2} - \hat{\mathbf{x}}_{2} \right) \right| \\
+ \mathbf{c}_{2} D^{1-\alpha} \left| \left(\mathbf{x}_{1} - \hat{\mathbf{x}}_{1} \right) \right| \right)$$

is bounded and sufficiently small, then we have $\dot{V} < 0$, the system is obtained globally and asymptotically stable.

Remark 4: In this study, the sign function in (30) is replaced by the saturation function to minimize the chattering



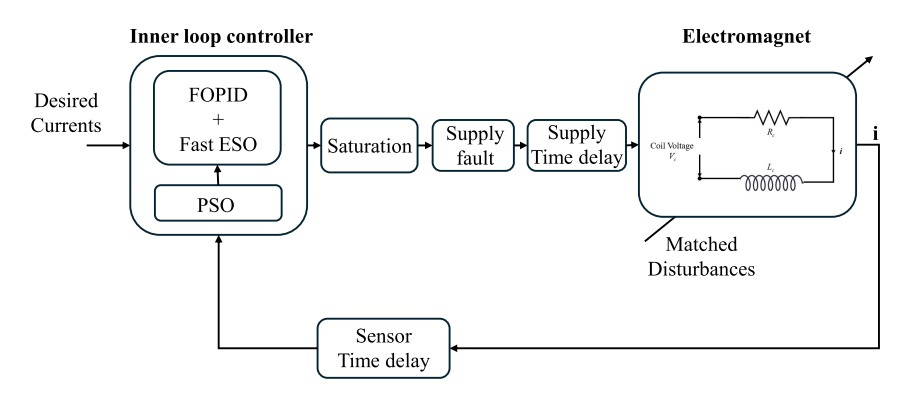


FIGURE 5. Control structure of Inner loop under time delays and supply faults.

phenomenon as follows:

$$\operatorname{sat}(\hat{\mathbf{s}}) = \begin{cases} \tanh(\hat{\mathbf{s}}), & \text{if } |\hat{\mathbf{s}}| \ge \kappa \\ \mathbf{s}, & \text{if } |\hat{\mathbf{s}}| < \kappa \end{cases}$$
(37)

where κ denotes the boundary layer, tanh is a hyperbolic function.

Remark 5: From (28), it can be seen that the fractionalorder integration of **e** is used to construct the sliding surface, it can be seen as a low-pass filter and can reduce the amplitude of high-frequency fluctuations of **e**. The robustness and efficiency of the proposed FOSMC approach are highlighted through the inclusion of two crucial terms:

- (i) The term $D^{1-\alpha}\mathbf{x_1}$ denotes the $(1-\alpha)$ th-order differentiation of $\mathbf{x_1}$, so the fractional dimension accelerating change of state error is contained in the output. As a result, the FOSMC method becomes more responsive to variations in state error, ensuring faster output adjustment.
- (ii) The other term is the $sgn(\hat{s})$ in (30) or the $sat(\hat{s})$ in (37), the former is a high-frequency switching signal, and the latter is a relatively smooth switch signal. According to the sliding surface s defined by (28), it is clear that an $(\alpha 1)$ th-order integrator for x_1 is contained, thus the fractional order sliding surface s is smoother than the conventional sliding surface. By using the FOSMC method, the chattering of $sgn(\hat{s})$ in (30) is eliminated to some degree, and the term $sat(\hat{s})$ in (37) is smoother.

B. INNER LOOP

The design of the controller must carefully balance the functionality of the closed-loop system in applications of CAMBs. While advanced integer-order controllers enhance reliability and flexibility, their complex structure and high computational requirements limit their practicality in industrial environments. Recently, fractional calculus has garnered significant attention for its ability to provide accurate dynamic system modeling, offering a broader perspective than traditional integral calculus.

Research utilizing eddy current evaluation suggests that fractionally ordered differential equations can more precisely represent the dynamic behavior of CAMBs compared to integer-order models. Fractional-order controllers, particularly in scenarios involving fractional-order differential equations, exhibit superior performance compared to integer-order controllers by accounting for the influence of eddy currents.

In recent years, the FOPID controller has been verified to be more effective than conventional PID controllers, especially in terms of robustness to system gain changes because of the flat phase constraint. For the inner loop control of the electrical part, we use the fractional-order PID controller expressed as follows [11]:

$$u(t) = k_p e(t) + k_i D^{-\lambda} + k_d D^{\mu} e(t)$$
 (38)

where e(t) is errors of the current of coils, u(t) are the output of the inner loop controller. Laplace transform of (38) can be calculated as follows:

$$C(s) = k_p + \frac{k_i}{s^{\lambda}} + k_d s^{\mu}$$
 (39)

where k_p , k_i , k_d , λ , and μ are the parameters to be tuned for the FOPID controller. The structure of the FOPID controller for the inner loop of CAMBs is described in Fig. 5. By using Hermite Biehler theorem, stabilizing sets of $PI^{\lambda}D^{\mu}$ controller for the plant with time delay are determined [2].

Remark 6: It should be highlighted that the conventional PID controller can be viewed as a particular case of the FOPID controller when $\lambda=1$ and $\mu=1$. By finetuning the two extra parameters of the FOPID controller, its performance can be significantly improved, surpassing the traditional PID controller for CAMBs.

Remark 7: Fractional-order PID controllers, when optimized using particle swarm optimization, have demonstrated their ability to satisfy essential requirements such as limiting current, minimizing overshoot, and enhancing response times. Moreover, they contribute to better system dynamics and steady-state characteristics, making them an attractive option for advancing control methodologies of CAMBs.

V. NUMERICAL SIMULATION STUDY

A. SIMULATION SETTINGS

In order to show the advantages of the HyESO-based fractional order approach proposed in this paper compared with the conventional sliding mode control and active



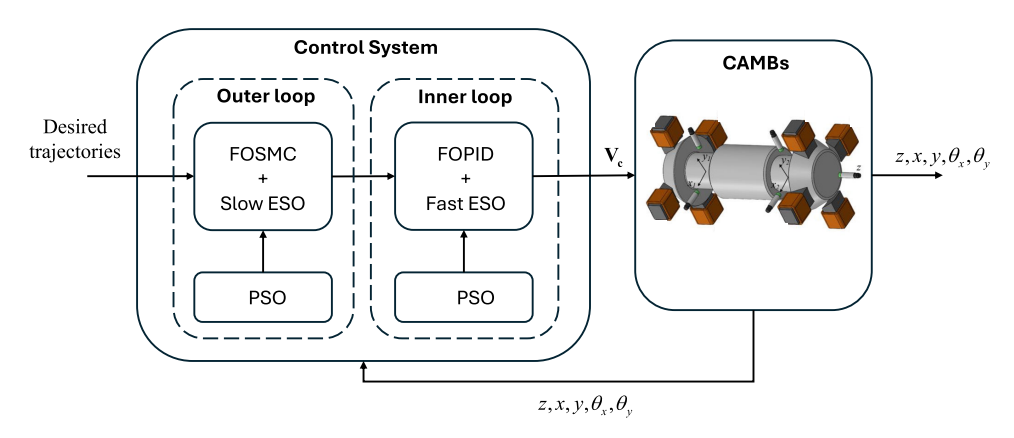


FIGURE 6. HyESO based cascaded position-current control.

disturbance rejection control (ADRC), we will use the MATLAB/Simulink environment to compare the performance, robustness, and effectiveness. The validation platform is implemented by the MATLAB R2024b environment using a fixed-step solver type and the Ode3 solver. The computer in the simulation is equipped with an Intel(R) Core(TM) i7-10850H CPU and 32 GB RAM, and fractional order calculus is solved by FOMCON Toolbox. The parameters of the object are as shown in the Table 1 [35]. In order to demonstrate the effectiveness of the proposed control system for CAMB, Scenario 1 for the inner loop and Scenario 2 with both outer loop and inner loop are presented as follows:

Scenario 1: Robustness of current loop under supply fault, input saturation, and time delay of sensor and supply. Structure of control system is given in Fig. 5

Control method: Four control systems are used to compare the performance and robustness for the inner loop. The control systems are included PID [35], FOPID [3], ESO-based PID [31] (i.e., PID-ESO), and the proposed control using ESO-based FOPID tuned by PSO (i.e., FOPID-ESO).

System Configuration: The parameter uncertainties, including ΔL_c and ΔR_c (i.e., the actual parameters of CAMBs deviate about 10% from the nominal value), lumped disturbances, input saturation, and time delay of sensor and supply are considered in this scenario. The matched disturbances are given as follows:

$$L_m = 100\sin(250t) \tag{40}$$

Scenario 1.1. The supply faults are not allowed to occur during the operation of the electromagnet.

Scenario 1.2. The supply faults are allowed to occur during the operation of the electromagnet. From (9), the loss of effectiveness and bias faults are taken into account as follows:

$$\rho(t) = 0.7 + 0.2\sin(20\pi t) \tag{41}$$

$$V_{fc} = 0.1\sin(30\pi t) \tag{42}$$

Scenario 2: Robustness of inner loop and outer loop under supply fault, input saturation, and time delay of sensor and supply. Structure of control system is given in Fig. 6.

Control method: Three control systems are used to compare the performance and robustness of the control

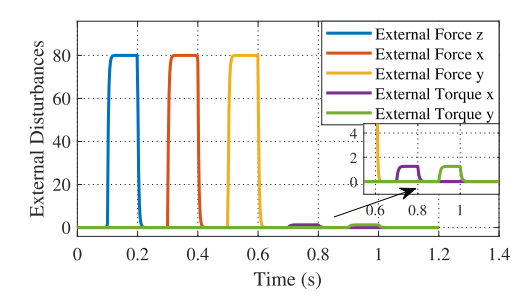


FIGURE 7. External disturbances acting on the rotor.

system, including the inner loop and outer loop. The control systems are given as controller 1 (i.e., ADRC [20] is applied for outer loop and PID [35] for inner loop), controller 2 is proposed by using ESO-based SMC [48] for outer loop and ESO-based PID [31] for inner loop, and the proposed fractional order controller 3 uses ESO-based FOSMC for outer loop and ESO-based FOPID, and all control parameters of Controller 3 are tuned by PSO.

System Configuration: The rotor is brought to the equilibrium position at the initial time. The conical active magnetic bearing is affected by the parameter uncertainties including ΔM , ΔG , and ΔK_c (i.e., the actual parameters of CAMBs deviate about 10% from the nominal value), the external disturbances as shown in Fig. 7, and the unbalance disturbance.

Scenario 2.1. The rotor of CAMBs rotates at high speed (3000 rpm) without unmodeled dynamics.

Scenario 2.2. Rotor of CAMBs rotates at very high speed (12,000 rpm) under unmodeled dynamics δ_z , δ_x , δ_y and δ_{θ_x} , δ_{θ_y} are given as follows:

$$\delta_z = \delta_x = \delta_y = 5\sin(100t) \tag{43}$$

$$\delta_{\theta_x} = \delta_{\theta_y} = 0.25 \sin(100t) \tag{44}$$

B. EVALUATION METHOD

To evaluate the effectiveness of the proposed method, not only the quantitative results but also the qualitative comparisons of tracking performance between the three controllers are also implemented, which consider



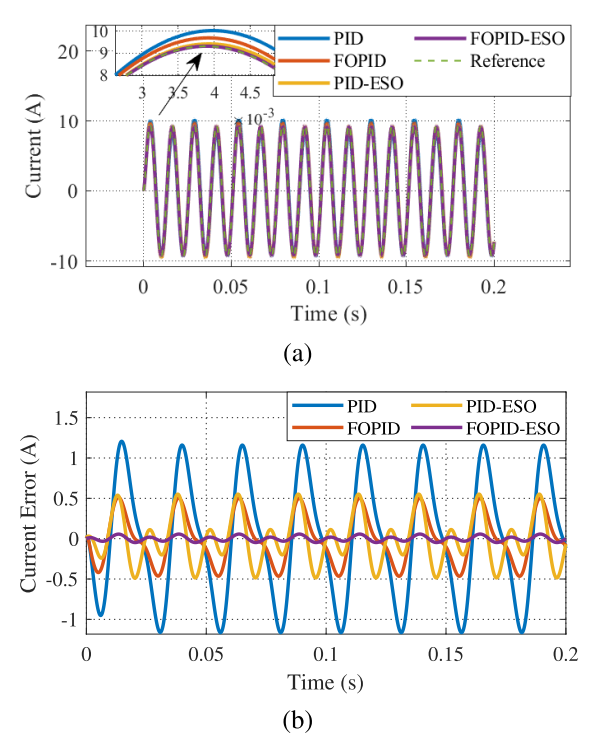
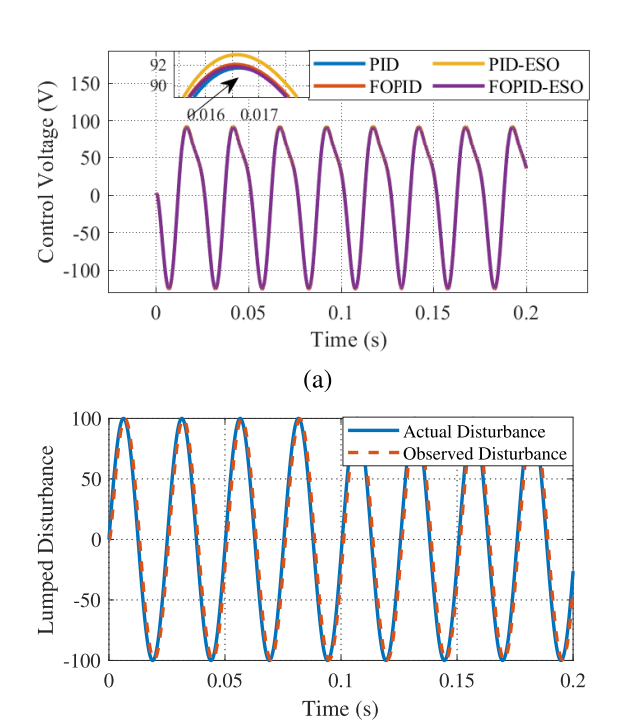


FIGURE 8. (a) Current responses of the controllers, (b) Current errors of the controllers (Scenario 1.1).



 $(b) \\ \label{eq:figure 9.}$ FIGURE 9. (a) Control voltage of the controllers, (b) Response of observed disturbance of the proposed system FOPID-ESO-PSO (Scenario 1.1).

performance metrics on displacement error, rotational angle error, and current error.

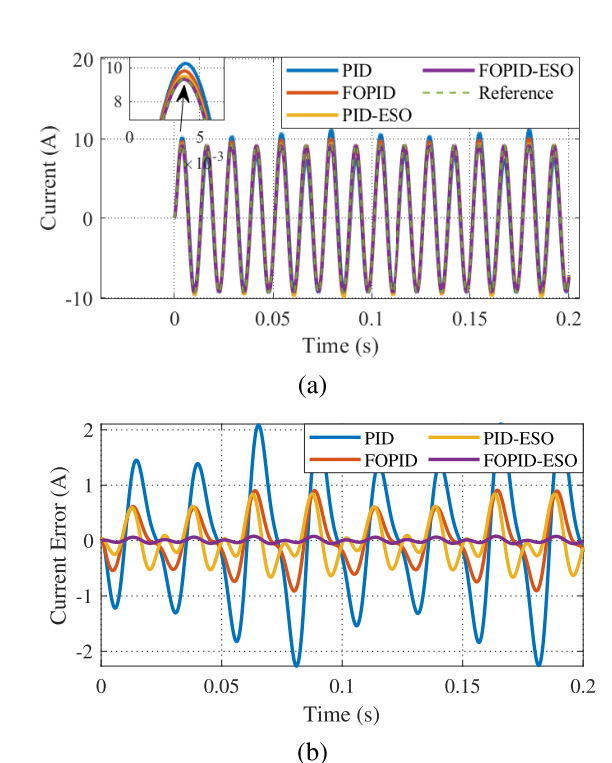


FIGURE 10. (a) Current responses of the controllers, (b) Current errors of the controllers (Scenario 1.2).

1) Integral squared errors (ISE)

$$ISE = \int_0^t e_\varrho^2(t)dt \tag{45}$$

2) Integral absolute errors (IAE)

$$IAE = \int_0^t \left| e_{\varrho}(t) \right| dt \tag{46}$$

3) Integral time-multiplied absolute errors (ITAE)

$$ITAE = \int_0^t t \left| e_{\varrho}(t) \right| dt \tag{47}$$

4) Root Mean Squared Error (RMSE)

RMSE =
$$\sqrt{\frac{1}{n} \sum_{i=1}^{n} e_i^2}$$
 (48)

5) Integral Time Squared Error (ITSE)

$$ITSE = \int_0^t te^2(t)dt \tag{49}$$

The ISE index penalizes a larger error than a smaller one, while the IAE index emphasizes the effect of error magnitude on the system's oscillation. The ITAE index prioritizes steady-state error over initial response, striking a balance between ISE and IAE. RMSE, on the other hand, evaluates the average deviation between actual and desired values, offering an intuitive measure of control accuracy and performance. ITSE emphasizes the importance of reducing errors over time, particularly penalizing errors that persist in later stages, thereby encouraging rapid stabilization of the



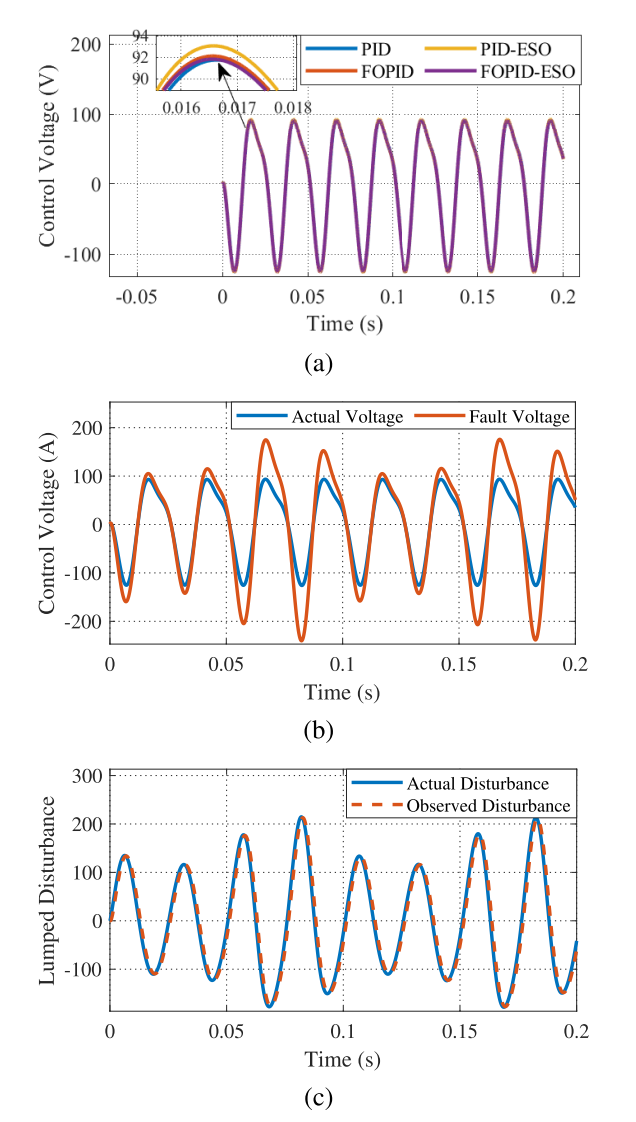


FIGURE 11. (a) Control voltage of the controllers, (b) Control voltage of the proposed system FOPID-ESO-PSO under supply fault, (c) Response of observed disturbance of the proposed system FOPID-ESO-PSO (Scenario 1.2).

system. It is worth noting that a lower value of these indices indicates a better control outcome.

To further improve the tracking performance of the proposed controller, the particle swarm optimization algorithm is employed to find the optimal controller and observer parameters. PSO is a powerful optimization algorithm inspired by the collective behaviour of swarms of birds or schools of fish. By iteratively updating the position and velocity of each particle in the swarm based on its current position and velocity, the particles in the swarm can gradually converge to the global best solution. Owing to its simplicity and stable convergence characteristics, PSO has been successfully applied to a variety of optimization tasks, including function optimization, parameter tuning, and energy power. Since the tracking performance of the controller mainly depends on the control gains of the controller and the observers of the inner loop and outer loop.

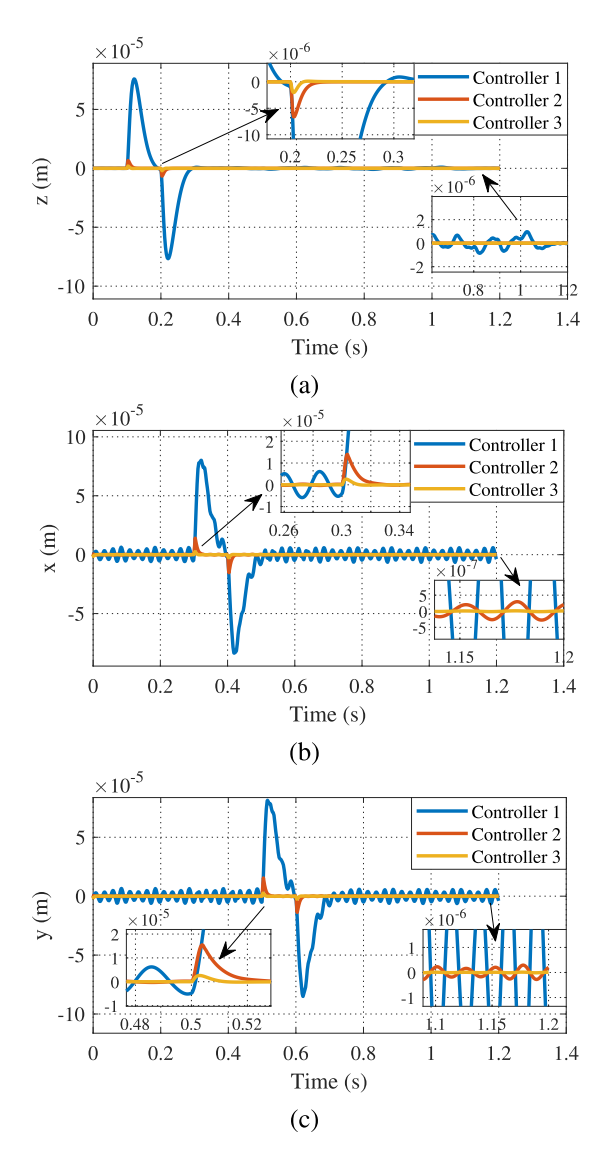


FIGURE 12. Transient response of rotor displacement: (a) Displacement *z*; (b) Displacement *x*; (c) Displacement *y* (Scenario 2.1).

The fitness function for PSO is defined based on the ITAE criteria as follows:

$$\min J = \int_0^t (w_1 t |e(t)| + w_2 t |u(t)|) dt$$
 (50)

where w_1, w_2 are weighting factors of errors and control input, respectively.

C. RESULT OF SCENARIO

1) RESULT OF SCENARIO 1

Scenario 1.1: Without supply faults.

This scenario demonstrates the effectiveness of the proposed controller FOPID-ESO-PSO to control the current of the inner loop under the influence of supply fault and time delay of supplies and sensors. In Fig. 8 shows the current response error of the controllers is shown; it can be seen that the errors of the controllers decrease in the order of PID, PID-ESO, FOPID, and FOPID-ESO. There, the error of FOPID is very good without using disturbance observation,



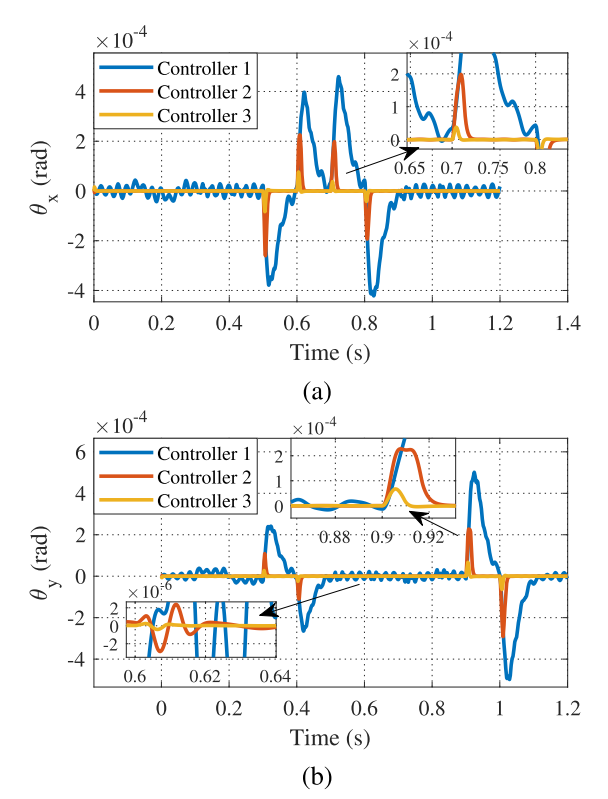


FIGURE 13. Transient response of rotor rotational angle: (a) Rotational angle θ_X ; (b) Rotational angle θ_Y (Scenario 2.1).

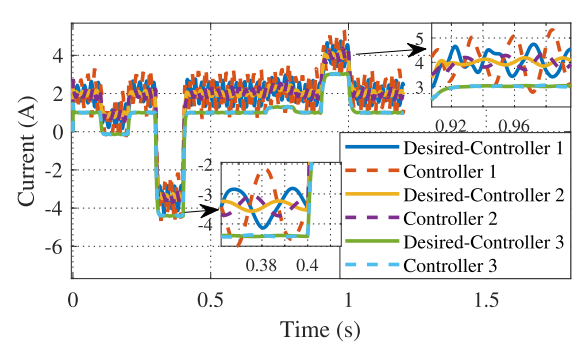


FIGURE 14. Current responses of the controllers (Scenario 2.1).

but the error is better than that of PID combined with ESO. Therefore, the proposed combination of ESO and PSO into FOPID has led to good results as Fig. 8b. The control voltage of the controllers is shown in Fig. 9a, and it is seen that the energy consumption of the 4 controllers is similar. Finally, for FOPID-ESO-PSO to achieve such good results, the observer has to work effectively when the lumped disturbance has both large amplitude and frequency as shown in Fig. 9b.

Scenario 1.2: Under supply faults

This scenario demonstrates the effectiveness of the proposed controller FOPID-ESO-PSO to control the current of the inner loop under the influence of supply fault and time delay of supplies and sensors. In which Fig. 10 shows the current response error of the controllers in scenario 1.2 when the system under the faults, it can be seen that the errors of the controllers decrease in the order of PID, PID-ESO, FOPID, FOPID-ESO. There, the error of FOPID is very

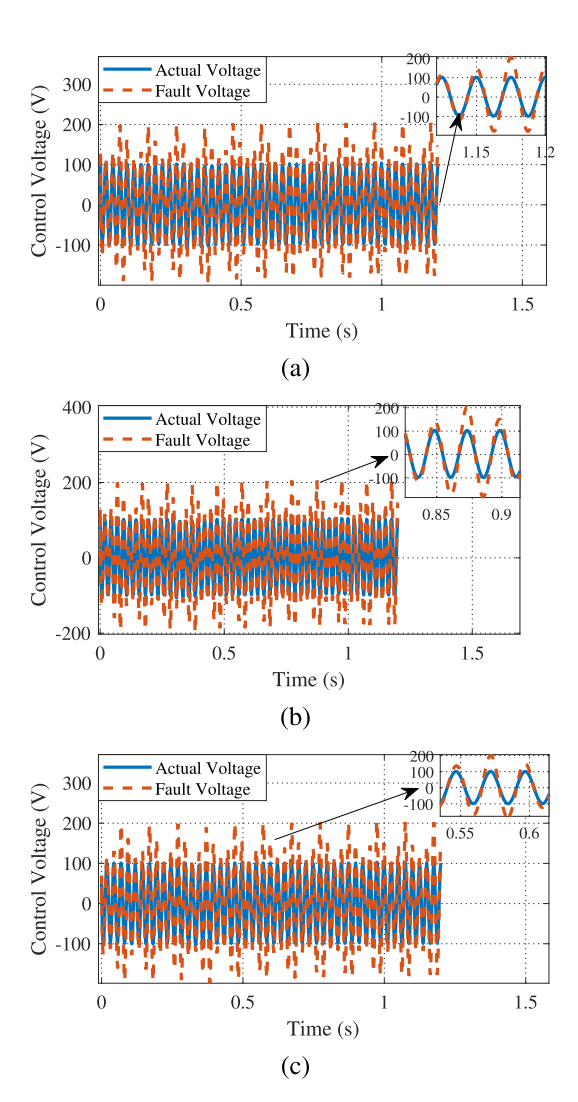


FIGURE 15. Control voltage of the controllers under supply fault: (a) Controller 1, (b) Controller 2, (c) Controller 3 (Scenario 2.1).

good without using disturbances observation, but the error is better than that of PID combined with ESO. Therefore, the proposed combination of ESO and PSO into FOPID has led to good results as Fig. 10b. The control voltage of the controllers is shown in Fig. 11a, and it is seen that the energy consumption of the 4 controllers is similar. Finally, for FOPID-ESO using PSO to achieve such good results, the observer has to work effectively when the lumped disturbance has both large amplitude and frequency, as shown in Fig. 11c. The supply fault phenomenon is clearly shown in Fig. 11b, when the output voltage cannot be achieved as the desired input voltage due to the influence of the fault.

2) RESULT OF SCENARIO 2

Scenario 2.1: Without unmodeled dynamics and operating in high speed 3000 rpm.

In this scenario, the rotor of CAMBs rotates at 3000 rpm without considering unmodeled dynamics. However, due to the influence of the external disturbance, supply faults, time delay, and parameter uncertainty, it causes a significant



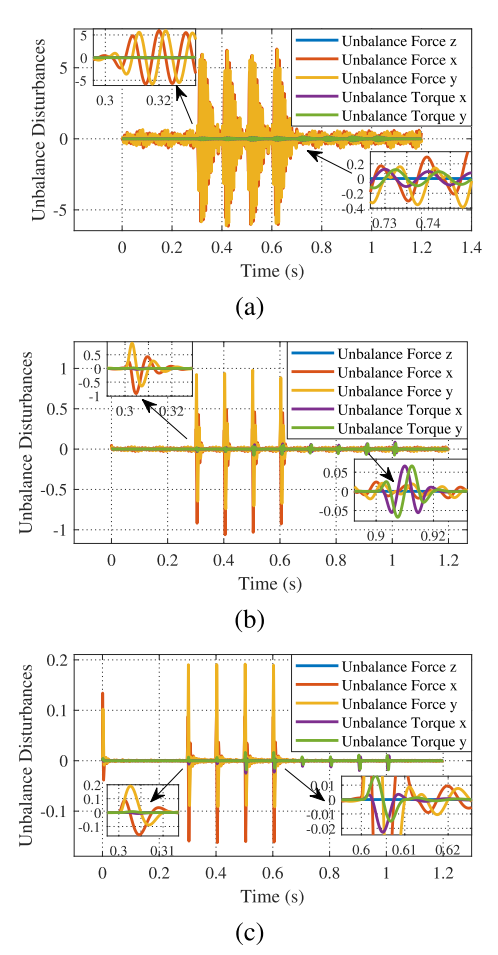


FIGURE 16. Unbalanced disturbances of the controllers: (a) Controller 1, (b) Controller 2, (c) Controller 3 (Scenario 2.1).

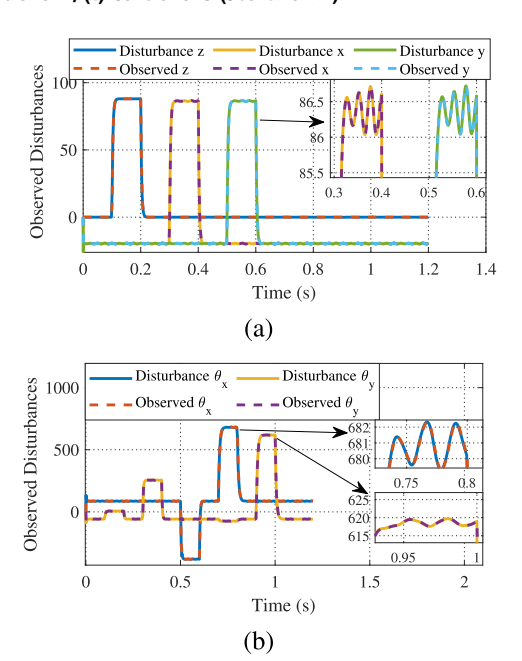


FIGURE 17. Response of observed disturbance of the proposed system: (a) Displacement z, x, y, (b) Rotational angle θ_X, θ_Y (Scenario 2.1).

impact on the response of the CAMBs. The transient response of rotor displacements and rotational angles of the three

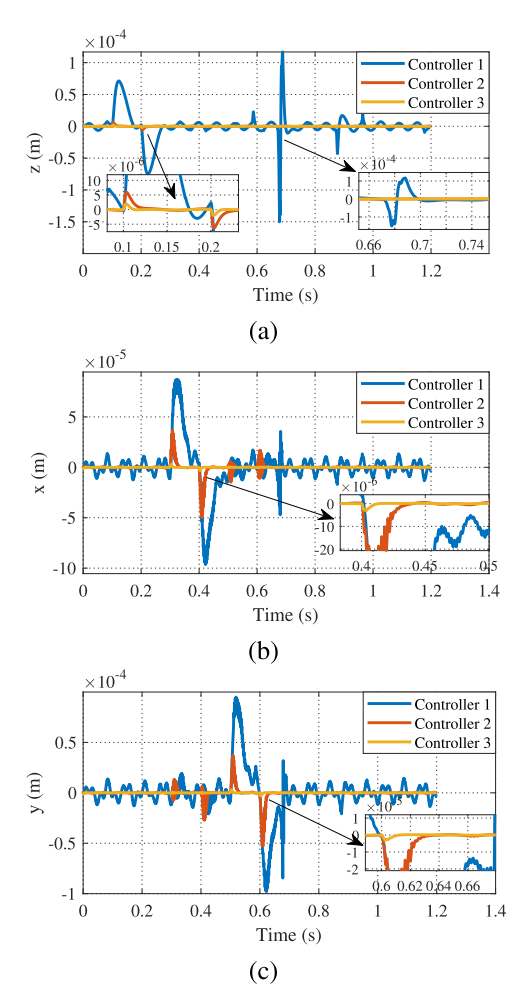


FIGURE 18. Transient response of rotor displacement: (a) Displacement *z*; (b) Displacement *x*; (c) Displacement *y* (Scenario 2.2).

controllers is shown in Fig.s 12-13. The proposed controllers 2 and 3 achieve the best results when the errors are very small in the situations of external disturbances and unmodeled dynamic impact.

It can be seen that due to the good control quality of controller 3, the unbalanced disturbances, as shown in Fig. 16, are also the smallest. From that, the current and voltage results of the controllers are shown in Fig. 14and Fig. 15. To achieve the effectiveness of controller 3, the observer has accurately observed the disturbances of displacements and rotational angles as shown in Fig. 17 under the uncertainty parameter, external disturbances in Fig. 7, and the unbalance disturbances in Fig. 16.

Scenario 2.2: Under unmodeled dynamics and operating very high speed of 12,000 rpm.

In this scenario, the rotor of CAMBs rotates at 12000 rpm without considering unmodeled dynamics. The transient response of rotor displacements and rotational angles of the three controllers is shown in Figs. 18-19. The proposed controller 3 achieves the best results when the errors are very small in situations of external disturbances and unmodeled dynamic impact. It can be seen that due to the good control



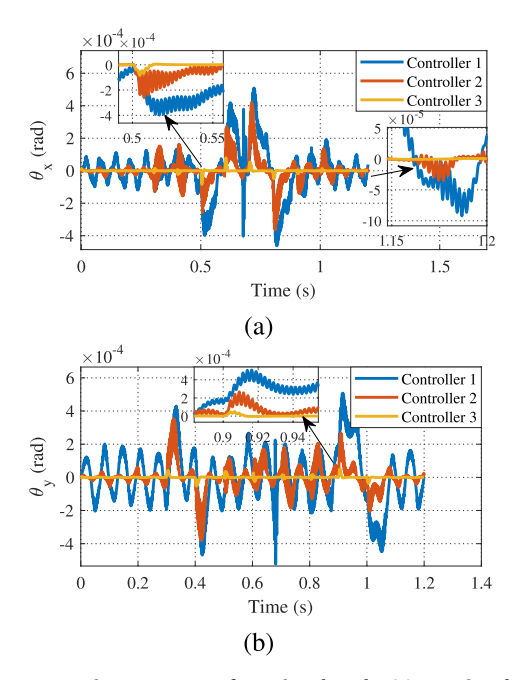


FIGURE 19. Transient response of rotational angle: (a) Rotational angle θ_X ; (b) Rotational angle θ_Y (Scenario 2.2).

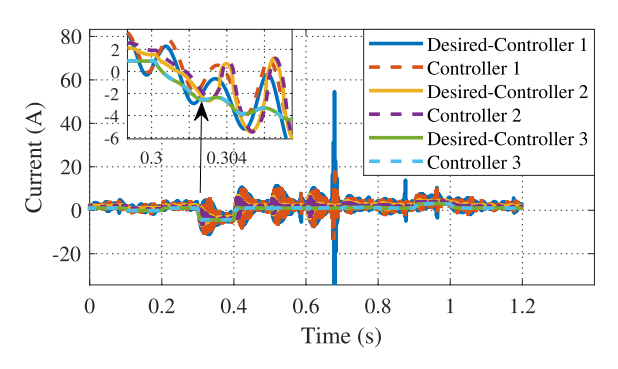


FIGURE 20. Current responses of the controllers (Scenario 2.2).

quality of controller 3, the unbalanced disturbances, as shown in Fig. 22, are also the smallest. From that, the current and voltage results of the controllers are shown in Fig. 20 and Fig. 21. To achieve the effectiveness of controller 3, the observer has accurately observed the disturbances of displacements and rotational angles as shown in Fig. 23 under the uncertainty parameter, external disturbances in Fig. 7, and the unbalance disturbances in Fig. 22.

D. DISCUSSION OF SCENARIO

For ease of presentation and tracking of results, we use a log scale to create bar charts. In addition, the percentage performance reduction compared to the column on the left is also displayed; detailed explanations will be presented in the following sub-subsections.

1) DISCUSSION OF SCENARIO 1

By using the performance indices as ISE, IAE, ITAE, RMSE, and ITSE (45)-(49), the effectiveness of the proposed

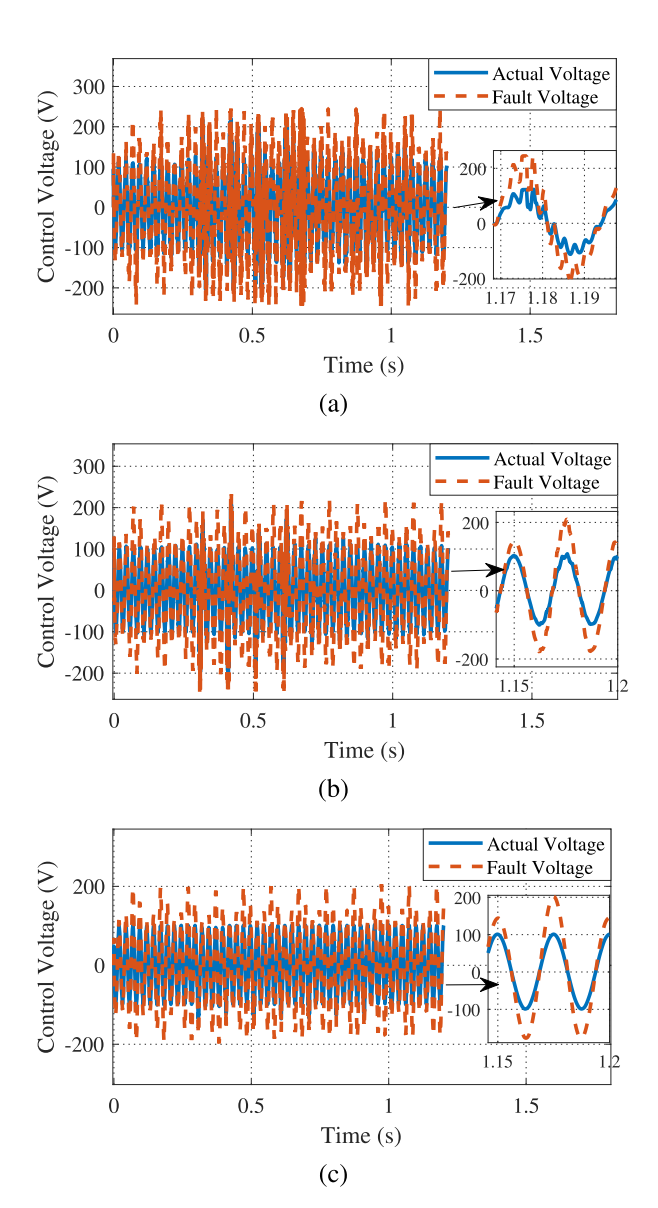


FIGURE 21. Control voltage of the controllers under supply fault: (a) Controller 1, (b) Controller 2, (c) Controller 3 (Scenario 2.2).

control structure is illustrated by the results of these metrics, which are shown in Figs. 24-25. The percentage shown on top of each column represents the reduction of this controller when evaluated compared to the adjacent left controller. For example, in Figure 24, when evaluating the ISE index, the performance index of FOPID decreased by 83.75% compared to PID, PID-ESO decreased by 1.78% compared to FOPID, and FOPID-ESO decreased by 98.93% compared to PID-ESO. Incorporating adjustable orders for both integration and differentiation of FOPID adds flexibility, enhances system adaptability, improves dynamic response, and reduces sensitivity to disturbances. Comparative analyses between PID, ESO-based PID, and FOPID have demonstrated that FOPID offers robustness and flexibility and achieves results that are equivalent to PID-ESO and superior to PID. As can be seen, the

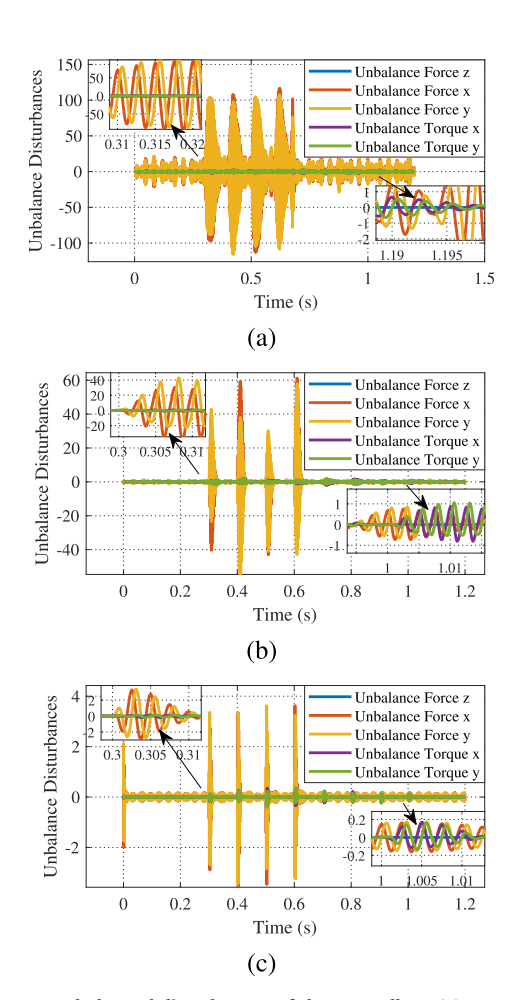


FIGURE 22. Unbalanced disturbances of the controllers: (a) Controller 1, (b) Controller 2, (c) Controller 3 (Scenario 2.2).

proposed method FOPID-ESO gives the smallest results in all performance metrics of the current response, which means that the proposed controller can provide stronger robustness and higher accuracy for the inner loop under the matched disturbances.

2) DISCUSSION OF SCENARIO 2

By using the performance indices as ISE, IAE, ITAE, RMSE, and ITSE (45)-(49), the effectiveness of the proposed control structure is illustrated by the results of these metrics, which are shown in Figs. 26-35. The percentage shown on top of each column represents the reduction of this controller when evaluated compared to the adjacent left controller. For example, in Figure 26, when evaluating the ITAE index, the performance index of controller 1 decreased by 99.90% compared to controller 1, controller 3 decreased by 73.66% compared to controller 2. Reading bar charts is similar to reading performance indicators and other figures. The results of scenario 2.1 are shown from Fig. 26-30, scenario 2.2 is from Fig. 31-35, we can generally comment that the response of the displacement z, x, y and the rotational angles θ_x , θ_y when comparing the proposed controller 2 with the

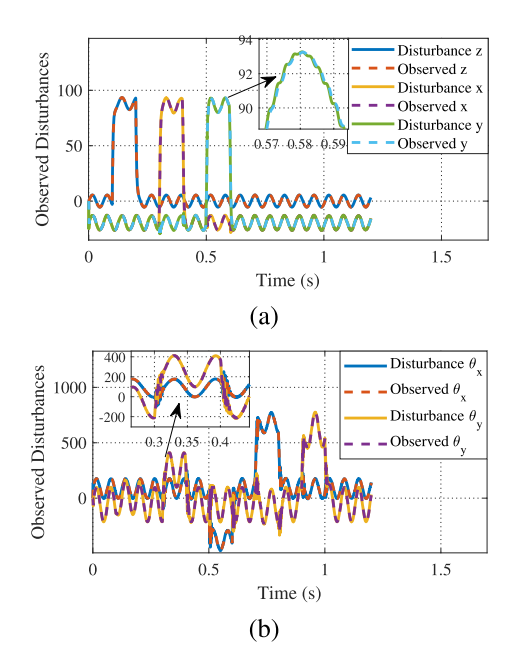


FIGURE 23. Response of observed disturbance of the proposed system: (a) Displacement z, x, y, (b) Rotational angle θ_X , θ_Y (Scenario 2.2).

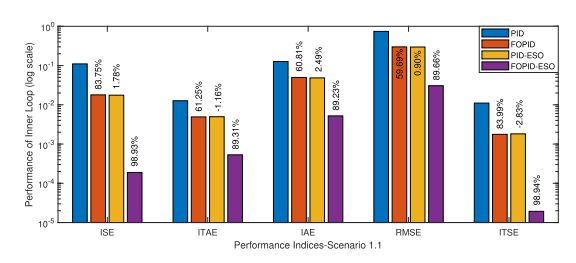


FIGURE 24. Performance of inner loop on log scale (Scenario 1.1).

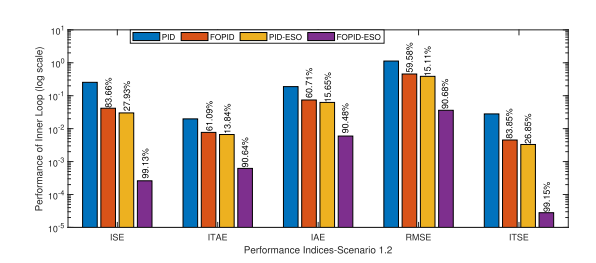


FIGURE 25. Performance of inner loop on log scale (Scenario 1.2).

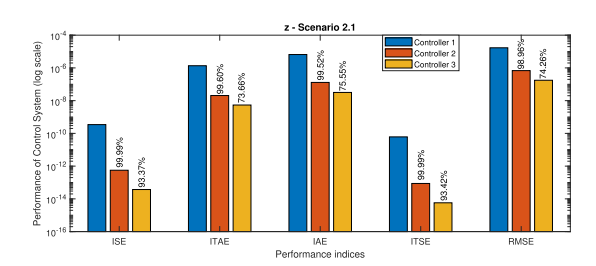


FIGURE 26. Performance of displacement z on log scale (Scenario 2.1).

standard controller using ADRC at the outer loop combined with PID at the inner loop has brought about superior



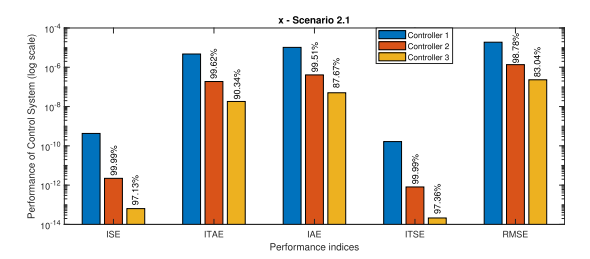


FIGURE 27. Performance of displacement x on log scale (Scenario 2.1).

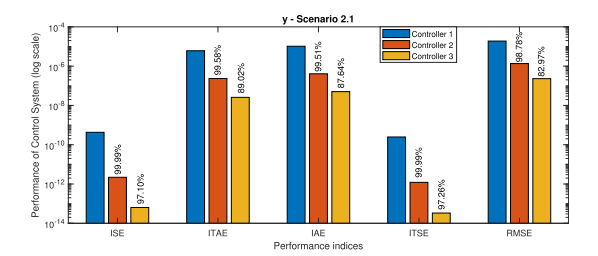


FIGURE 28. Performance of displacement y on log scale (Scenario 2.1).

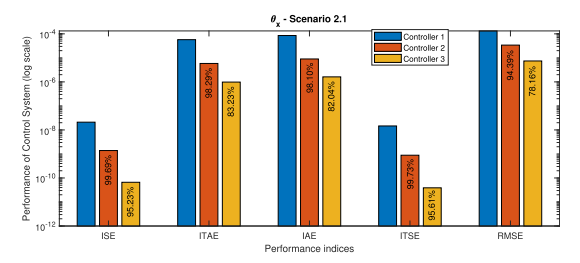


FIGURE 29. Performance of rotational angle θ_X on log scale (Scenario 2.1).

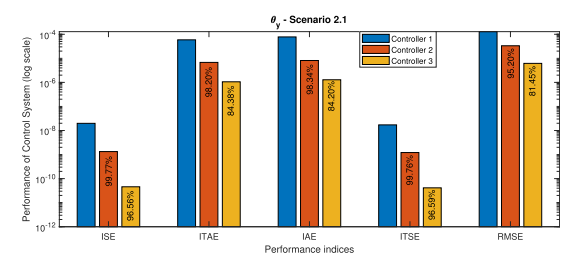


FIGURE 30. Performance of rotational angle θ_V on log scale (Scenario 2.1).

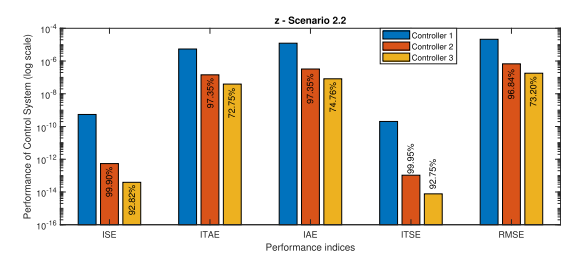


FIGURE 31. Performance of displacement z on log scale (Scenario 2.2).

results. In addition, another control structure we proposed, controller 3, once again achieved superior results when compared with controller 2. As can be seen, the proposed method gives the smallest results in all performance metrics

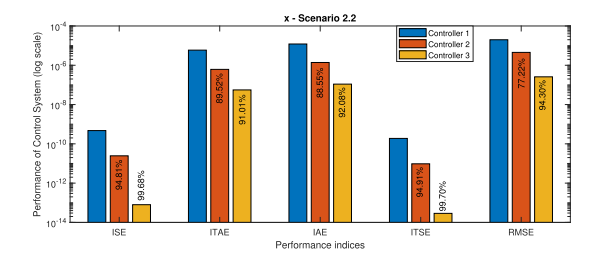


FIGURE 32. Performance of displacement x on log scale (Scenario 2.2).

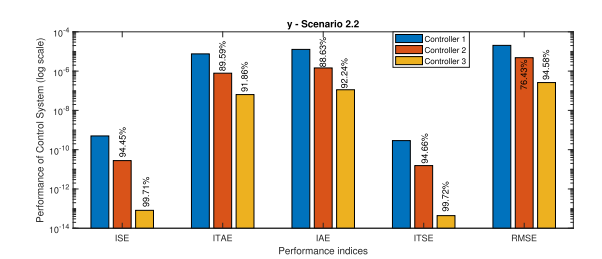


FIGURE 33. Performance of displacement y on log scale (Scenario 2.2).

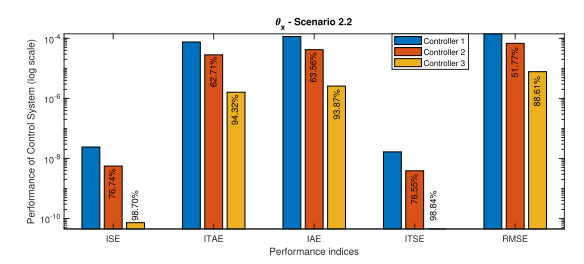


FIGURE 34. Performance of rotational angle θ_X on log scale (Scenario 2.2).

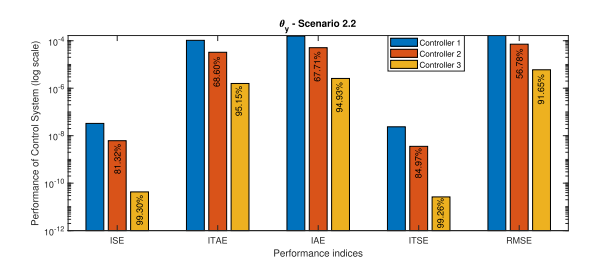


FIGURE 35. Performance of rotational angle θ_y on log scale (Scenario 2.2).

of the displacements and the rotational angles, which means that the proposed controller 3 and controller 2 can provide stronger robustness and higher accuracy for CAMBs under the mismatched and matched disturbances.

VI. CONCLUSION

In this study, the detailed mathematical model, as well as the design of a highly accurate control scheme, is proposed under the influence of external disturbances, unbalanced disturbances, and supply faults. The proposed mathematical model integrates both the electrical and mechanical systems, making it subject to mismatched and matched disturbances. Furthermore, the system also accounts for issues such as supply faults, supply saturation, and time delays in both power supplies and sensors. The cascade control structure



for CAMBs is proposed, comprising an outer loop and an inner loop. The outer loop employs fractional sliding mode control to regulate the rotor's displacement and rotational angle. Meanwhile, the inner loop utilizes a fractional-order PID controller to control coil currents, effectively mitigating the time delay issues associated with power supplies and sensors. Finally, disturbances are addressed through the hybrid extended state observer structure, where the fast ESO is implemented in the inner loop, while the slow ESO is applied to the outer loop to observe mismatched and matched disturbances.

Further research may include real-time testing of the CAMBs in various applications such as flywheels, air compressors, and others to validate the controller's stability and effectiveness.

DECLARATION OF COMPETING INTEREST

The authors declare that they have no known competing financial interests or personal relationships that could have appeared to influence the work reported in this article.

APPENDIX

The details of the matrices M, G, K_i , K_d of the paper are presented in detail as follows:

 $K_{14} = -K_{15} = (b_1 + b_2)(K_{q_1} - K_{q_2})\sin\beta\cos\beta$

$$K_{22} = K_{33} = 2\cos^{2}\beta(K_{q_{1}} + K_{q_{2}})$$

$$K_{25} = K_{52} = -K_{34} = -K_{43} = \cos^{2}\beta(K_{q_{1}} + K_{q_{2}})$$

$$\times (b_{1} - b_{2})$$

$$K_{41} = -K_{51} = \sin\beta(K_{q_{1}} - K_{q_{2}}) [(b_{1} + b_{2})\cos\beta$$

$$-2R_{m}\sin\beta)]$$

$$K_{44} = K_{55} = \cos\beta(K_{q_{1}} + K_{q_{2}}) [(b_{1}^{2} + b_{2}^{2})\cos\beta$$

$$-R_{m}(b_{1} + b_{2})\cos\beta)]$$

The details of (4) are presented as follows:

$$\begin{bmatrix} i_{y1} \\ i_{y2} \\ i_{y3} \\ i_{y4} \\ i_{x1} \\ i_{x2} \\ i_{x3} \\ i_{x4} \end{bmatrix} = \underbrace{\begin{bmatrix} I_{01} \\ I_{02} \\ I_{01} \\ I_{02} \\ I_{01} \\ I_{02} \end{bmatrix}}_{\mathbf{I}_{0}} + \underbrace{\begin{bmatrix} 1 & 0 & 0 & 0 & 1 \\ 1 & 0 & 0 & 0 & -1 \\ -1 & 0 & 1 & 0 & 0 \\ -1 & 0 & -1 & 0 & 0 \\ 1 & 0 & 0 & -1 & 0 \\ -1 & 1 & 0 & 0 & 0 \\ -1 & 1 & 0 & 0 & 0 \end{bmatrix}}_{\mathbf{I}_{2}} \underbrace{\begin{bmatrix} I_{z} \\ I_{x1} \\ I_{y1} \\ I_{x2} \\ I_{y2} \end{bmatrix}}_{\mathbf{i}_{r}}$$

ACKNOWLEDGMENT

The authors acknowledge TU Wien Bibliothek for financial support through its Open Access Funding Programme. This research is funded by the Hanoi University of Science and Technology (HUST) under project number T2023-PC-029.

REFERENCES

- M. Abu-Shady and M. K. A. Kaabar, "A generalized definition of the fractional derivative with applications," *Math. Problems Eng.*, vol. 2021, Oct. 2021, Art. no. 9444803.
- [2] D. S. Acharya, S. K. Mishra, S. K. Swain, and S. Ghosh, "Real-time implementation of fractional-order PID controller for magnetic levitation plant with time delay," *IEEE Trans. Instrum. Meas.*, vol. 71, pp. 1–11, 2022.
- [3] P. Anantachaisilp and Z. Lin, "Fractional order PID control of rotor suspension by active magnetic bearings," *Actuators*, vol. 6, no. 1, p. 4, Jan. 2017.
- [4] A. Atangana and A. Seçer, "A note on fractional order derivatives and table of fractional derivatives of some special functions," *Abstract Appl. Anal.*, vol. 2013, Jan. 2013, Art. no. 279681.
- [5] A. Bonfitto, N. Amati, L. D. Suarez, and A. Tonoli, "Turbomolecular pumps on conical active magnetic bearings," *Mech. Eng. J.*, vol. 4, no. 5, 2017, Art. no. 1600569.
- [6] A. Bonfitto, A. Tonoli, G. Botto, M. Silvagni, and L. D. Suarez, "Rotor on cone-shaped active magnetic bearings with three-phases power drivers," in *Proc. 13th Int. Symp. Magn. Bearings*, Jan. 2012, pp. 513–526.
- [7] L. M. C. Molina, R. Galluzzi, A. Bonfitto, S. Circosta, and R. A. Ramírez-Mendoza, "Grey-box identification of a cone-shaped active magnetic bearing system," in *Proc. 3rd Latin Amer. Congr. Autom. Robot. Adv. Autom. Robot. Res.* Cham, Switzerland: Springer, Nov. 2021, pp. 148–163.
- [8] V. T. Dang, D. B. H. Nguyen, T. D. T. Tran, D. T. Le, and T. L. Nguyen, "Model-free hierarchical control with fractional-order sliding surface for multisection web machines," *Int. J. Adapt. Control Signal Process.*, vol. 37, no. 2, pp. 497–518, Feb. 2023.
- [9] S. Dey, S. Banerjee, and J. Dey, "Practical application of fractional-order PID controller based on evolutionary optimization approach for a magnetic levitation system," *IETE J. Res.*, vol. 69, no. 11, pp. 8168–8192, Nov. 2023.
- [10] A. Dumlu, "Design of a fractional-order adaptive integral sliding mode controller for the trajectory tracking control of robot manipulators," *Proc. Inst. Mech. Eng., I, J. Syst. Control Eng.*, vol. 232, no. 9, pp. 1212–1229, Oct. 2018.



- [11] D. Dutta, P. K. Biswas, S. Debnath, and F. Ahmad, "Advancements and challenges in active magnetic bearings: A comprehensive review of performance, control, and future prospects," *IEEE Access*, vol. 13, pp. 3051–3071, 2025.
- [12] J. Fang, C. Wang, and J. Tang, "Modeling and analysis of a novel conical magnetic bearing for Vernier-gimballing magnetically suspended flywheel," *Proc. Inst. Mech. Eng., C, J. Mech. Eng. Sci.*, vol. 228, no. 13, pp. 2416–2425, Sep. 2014.
- [13] R. V. Gandhi and D. M. Adhyaru, "Feedback linearization based optimal controller design for electromagnetic levitation system," in *Proc. Int. Conf. Control, Instrum., Commun. Comput. Technol. (ICCICCT)*, Dec. 2016, pp. 36–41.
- [14] R. V. Gandhi and D. M. Adhyaru, "Hybrid extended state observer based control for systems with matched and mismatched disturbances," *ISA Trans.*, vol. 106, pp. 61–73, Nov. 2020.
- [15] R. V. Gandhi, D. M. Adhyaru, and J. Kasundra, "Modeling of current and voltage controlled electromagnetic levitation system based on novel approximation of coil inductance," in *Proc. 4th Int. Conf. Control, Autom. Robot. (ICCAR)*, Apr. 2018, pp. 212–217.
- [16] P. Gao, G. Zhang, and X. Lv, "A novel compound nonlinear state error feedback super-twisting fractional-order sliding mode control of PMSM speed regulation system based on extended state observer," *Math. Problems Eng.*, vol. 2020, pp. 1–15, Jun. 2020.
- [17] Q. Gao, Y. Hou, J. Liu, R. Hou, M. Lv, L. Wang, and C. Wang, "An extended state observer based fractional order sliding-mode control for a novel electro-hydraulic servo system with iso-actuation balancing and positioning," *Asian J. Control*, vol. 21, no. 1, pp. 289–301, Sep. 2018.
- [18] S.-J. Huang and L.-C. Lin, "Fuzzy modeling and control for conical magnetic bearings using linear matrix inequality," *J. Intell. Robotic Syst.*, vol. 37, no. 2, pp. 209–232, Jun. 2003.
- [19] B. Jin, Fractional Differential Equations (Applied Mathematical Sciences), vol. 206, no. 2. Cham, Switzerland: Springer, 2021, pp. 155–159, doi: 10.1007/978-3-030-76043-4. [Online]. Available: https://link.springer.com/10.1007/978-3-030-76043-4
- [20] C. Jin, K. Guo, Y. Xu, H. Cui, and L. Xu, "Design of magnetic bearing control system based on active disturbance rejection theory," *J. Vibrat. Acoust.*, vol. 141, no. 1, Feb. 2019, Art. no. 011009.
- [21] Y. Jing, Y. Lie, and X. Jing, "Coupled dynamics and control of a rotor-conical magnetic bearing system," *Proc. Inst. Mech. Eng., J, J. Eng. Tribol.*, vol. 220, no. 7, pp. 581–586, Jul. 2006.
- [22] A. Katyayn and P. K. Agarwal, "Comparative analysis of conical and conventional active magnetic bearings for complete support of a 5-DOF rotor system," in *Proc. Int. Conf. Adv. Mech., Ind., Autom. Manage. Syst.* (AMIAMS), Feb. 2017, pp. 53–58.
- [23] A. Katyayn and P. K. Agarwal, "Type-2 fuzzy logic controller for conical AMB-rotor system," in *Proc. 4th Int. Conf. Power, Control Embedded Syst.* (ICPCES), Mar. 2017, pp. 1–6.
- [24] M. N. Kumar and R. Chidanandappa, "Particle swarm optimization technique for speed control and torque ripple minimization of switched reluctance motor using PID and FOPID controllers," *Int. J. Inf. Technol.*, vol. 16, no. 2, pp. 1185–1201, Feb. 2024.
- [25] V. Kumarasamy, V. K. Ramasamy, G. Chandrasekaran, G. Chinnaraj, P. Sivalingam, and N. S. Kumar, "A review of integer order PID and fractional order PID controllers using optimization techniques for speed control of brushless DC motor drive," *Int. J. Syst. Assurance Eng. Manage.*, vol. 14, no. 4, pp. 1139–1150, Aug. 2023.
- [26] J. Laldingliana and P. K. Biswas, "Artificial intelligence based fractional order PID control strategy for active magnetic bearing," *J. Electr. Eng. Technol.*, vol. 17, no. 9, pp. 3389–3398, May 2022.
- [27] N. H. Le, T. Q. Ngo, D. K. Hoang, Q. D. Nguyen, D. T. Le, and T. L. Nguyen, "Robust adaptive cerebellar model articulation controller for 1-DOF nonlaminated active magnetic bearings," *Tehnički vjesnik*, vol. 30, no. 5, pp. 1411–1418, 2023.
- [28] C.-W. Lee and H.-S. Jeong, "Dynamic modeling and optimal control of cone-shaped active magnetic bearing systems," *Control Eng. Pract.*, vol. 4, no. 10, pp. 1393–1403, Oct. 1996.
- [29] F.-J. Lin, S.-Y. Chen, and M.-S. Huang, "Intelligent double integral sliding-mode control for five-degree-of-freedom active magnetic bearing system," *IET Control Theory Appl.*, vol. 5, no. 11, pp. 1287–1303, Jul 2011.
- [30] L.-C. Lin and T.-B. Gau, "Feedback linearization and fuzzy control for conical magnetic bearings," *IEEE Trans. Control Syst. Technol.*, vol. 5, no. 4, pp. 417–426, Jul. 1997.

- [31] C. Liu, G. Liu, and J. Fang, "Feedback linearization and extended state observer-based control for rotor-AMBs system with mismatched uncertainties," *IEEE Trans. Ind. Electron.*, vol. 64, no. 2, pp. 1313–1322, Feb. 2017.
- [32] K. Michail, A. C. Zolotas, and R. M. Goodall, "Optimised sensor selection for control and fault tolerance of electromagnetic suspension systems: A robust loop shaping approach," ISA Trans., vol. 53, no. 1, pp. 97–109, Jan. 2014.
- [33] A. M. Mohamed and F. P. Emad, "Conical magnetic bearings with radial and thrust control," in *Proc. 28th IEEE Conf. Decis. Control*, Jun. 1989, pp. 554–561.
- [34] F. Mohd Zaihidee, S. Mekhilef, and M. Mubin, "Robust speed control of PMSM using sliding mode control (SMC)—A review," *Energies*, vol. 12, no. 9, p. 1669, May 2019.
- [35] L. M. Castellanos Molina, A. Bonfitto, and R. Galluzzi, "Offset-free model predictive control for a cone-shaped active magnetic bearing system," *Mechatronics*, vol. 78, Oct. 2021, Art. no. 102612.
- [36] D. H. Nguyen, T. T. Ta, L. M. Vu, V. T. Dang, D. G. Nguyen, D. T. Le, D. D. Nguyen, and T. L. Nguyen, "Fractional order active disturbance rejection control for canned motor conical active magnetic bearingsupported pumps," *Inventions*, vol. 8, no. 1, p. 15, Jan. 2023.
- [37] D. H. Nguyen, M. Le Vu, H. D. Trong, D. G. Nguyen, and T. L. Nguyen, "Active disturbance rejection control-based anti-coupling method for conical magnetic bearings," *Acta Polytechnica*, vol. 62, no. 4, pp. 479–487, Aug. 2022, doi: 10.14311/AP.2022.62.0479. [Online]. Available: https://ojs.cvut.cz/ojs/index.php/ap/article/view/7523
- [38] S. Palis, M. Stamann, and T. Schallschmidt, "Nonlinear adaptive control of magnetic bearings," in *Proc. Eur. Conf. Power Electron. Appl.*, Jan. 2007, pp. 1–10.
- [39] S. N. Pawar, R. H. Chile, and B. M. Patre, "Design of generalized extended state observer based control for nonlinear systems with matched and mismatched uncertainties," in *Proc. Indian Control Conf. (ICC)*, Jan. 2017, pp. 65–71.
- [40] S. Saha, S. M. Amrr, and M. Nabi, "Adaptive second order sliding mode control for the regulation of active magnetic bearing," *IFAC-PapersOnLine*, vol. 53, no. 1, pp. 1–6, 2020.
- [41] S. Saha, S. M. Amrr, A. S. Saidi, A. Banerjee, and M. Nabi, "Finite-time adaptive higher-order SMC for the nonlinear five DOF active magnetic bearing system," *Electronics*, vol. 10, no. 11, p. 1333, Jun. 2021.
- [42] A. Saxena, Y. M. Dubey, M. Kumar, and A. Saxena, "Performance comparison of ANFIS, FOPID-PSO and FOPID-fuzzy tuning methodology for optimizing response of high-performance drilling machine," *IETE J. Res.*, vol. 69, no. 6, pp. 3497–3510, Jun. 2021.
- [43] A. M. A.-H. Shata, R. A. Hamdy, A. S. Abdelkhalik, and I. El-Arabawy, "A fractional order PID control strategy in active magnetic bearing systems," *Alexandria Eng. J.*, vol. 57, no. 4, pp. 3985–3993, Dec. 2018.
- [44] Z. Wei, B. Zhang, and Y. Jiang, "Analysis and modeling of fractional-order buck converter based on Riemann–Liouville derivative," *IEEE Access*, vol. 7, pp. 162768–162777, 2019.
- [45] S. Xu and J. Fang, "A novel conical active magnetic bearing with claw structure," *IEEE Trans. Magn.*, vol. 50, no. 5, pp. 1–8, May 2014.
- [46] J. Yang, A. Zolotas, W.-H. Chen, K. Michail, and S. Li, "Robust control of nonlinear MAGLEV suspension system with mismatched uncertainties via DOBC approach," *ISA Trans.*, vol. 50, no. 3, pp. 389–396, Jul. 2011.
- [47] S. Yu, Y. Feng, and X. Yang, "Extended state observer-based fractional order sliding-mode control of piezoelectric actuators," *Proc. Inst. Mech. Eng.*, *I, J. Syst. Control Eng.*, vol. 235, no. 1, pp. 39–51, Jul. 2020.
- [48] Z. Yu, Y. Tang, B. Xu, X. Huang, and H.-T. Zhang, "Linear extended state observer-based sliding mode control of active magnetic bearing systems," in *Proc. 41st Chin. Control Conf. (CCC)*, Jul. 2022, pp. 710–714.



DUC THINH LE received the B.S. and M.S. degrees in control and automation engineering from Hanoi University of Science and Technology, Hanoi, Vietnam, in 2021 and 2023, respectively. He is currently a Lecturer with the Faculty of Electrical and Electronics Engineering, Thuyloi University. His current research interests include electric drives, electric vehicles, motion control, and modeling and simulation.





DANH GIANG NGUYEN received the B.S. and M.S. degrees in control and automation engineering from Hanoi University of Science and Technology, Hanoi, Vietnam, in 2013 and 2017, respectively. He is currently a Lecturer with the Department of Faculty of Mechanical Engineering, Hanoi University of Civil Engineering.



MINH VU NHAT received the M.S. degree from Korea Institute of Science and Technology, in 2017, and the Ph.D. degree from TU Wien, in 2023. He is currently a Postdoctoral Researcher with the Automation and Control Institute (ACIN) and a Scientist with the Austrian Institute of Technology (AIT) GmbH. His research interests include robotics, control, and optimization.



THE TAI TA received the B.S. and M.S. degrees in control and automation engineering from Hanoi University of Science and Technology, Hanoi, Vietnam, in 2021 and 2023, respectively. His research interests include active magnetic bearings, control, and optimization.



TUNG LAM NGUYEN (Senior Member, IEEE) received the B.S. degree in control and automation engineering from Hanoi University of Science and Technology, Vietnam, in 2005, the M.S. degree from the Asian Institute of Technology, Thailand, in 2007, and the Ph.D. degree from The University of Western Australia, Australia, in 2014. He has been appointed as an Associate Professor of control engineering and automation. He is currently a Lecturer with the Department

of Industrial Automation, School of Electrical and Electronic Engineering, Hanoi University of Science and Technology. His research interests include motion control, control systems, and their applications.



DANH HUY NGUYEN received the B.S., M.S., and Ph.D. degrees in control and automation engineering from Hanoi University of Science and Technology, Hanoi, Vietnam, in 1997, 1999, and 2019, respectively. He is currently a Lecturer with the School of Electrical and Electronic Engineering, Hanoi University of Science and Technology.

. . .